

MORPHOLOGIES OF $\sim 190,000$ GALAXIES AT $z = 0 - 10$ REVEALED WITH HST LEGACY DATA. III. CONTINUUM PROFILE AND SIZE EVOLUTION OF LY α EMITTERS

TAKATOSHI SHIBUYA^{1,2}, MASAMI OUCHI^{2,3}, YUICHI HARIKANE^{2,4}, AND KIMIHIKO NAKAJIMA⁵

Submitted to ApJ, 2018 September 4; accepted 2018 December 3

ABSTRACT

We present the redshift evolution of the radial surface brightness (SB) profile of the rest-frame UV and optical stellar continua for 9119 Ly α emitters (LAEs) at $z \simeq 0 - 8$ and $0 - 2$, respectively. Using *Hubble Space Telescope* data and the LAE catalogs taken from the literature, we derive the structural quantities of the 9119 LAEs and $\simeq 180,000$ comparison galaxies of photo- z star-forming galaxies (SFGs) and Lyman break galaxies (LBGs) by the well-tested profile fitting. From 936 well-fitted LAEs, we carefully define the homogeneous sample of LAEs falling in the same ranges of UV-continuum luminosity and Ly α equivalent width over $z \simeq 0 - 8$, and evaluate the redshift evolution. We find that the effective radius r_e distribution is represented by a log-normal function, and that the median Sérsic index is almost constant at $n \simeq 1 - 1.5$ for the LAEs over $z \simeq 0 - 7$, suggesting that typical LAEs have a stellar-disk morphology. The size-luminosity relation of the LAEs monotonically decreases towards high- z , following size-luminosity relations of SFGs and LBGs. The median r_e values of the LAEs significantly evolve as $r_e \propto (1+z)^{-1.37}$, similar to those of the SFGs and LBGs in the same luminosity range, in contrast with the claims of no evolution made by previous studies whose LAE samples are probably biased to faint sources at low- z . The r_e distribution, star-formation rate surface densities, and stellar-to-halo size ratios of the LAEs are comparable with those of the SFGs and LBGs, indicating that LAEs have stellar components similar to SFGs and LBGs with a Ly α emissivity controlled by the non-stellar physics such as geometry, kinematics, and ionization states of the inter-stellar/circum-galactic medium.

Subject headings: cosmology: observations — early universe — galaxies: formation — galaxies: high-redshift

1. INTRODUCTION

Galaxy morphological properties provide us with invaluable hints for understanding the galaxy formation and evolution mechanisms. Particularly, radial surface brightness (SB) profiles and angular sizes of galaxies contain a lot of crucial information about e.g., galaxy build-up processes and the relation between stellar components and underlying dark matter (DM) halos. These key morphological quantities are studied extensively with high spatial resolution images of the *Hubble Space Telescope* (*HST*) for star-forming galaxies (SFGs), quiescent galaxies (e.g., Shen et al. 2003; van der Wel et al. 2014) and Lyman break galaxies (LBGs) up to redshift $z \simeq 10$ (e.g., Bouwens et al. 2004; Grazian et al. 2012; Huang et al. 2013; McLure et al. 2013; Ono et al. 2013; Shibuya et al. 2015; Holwerda et al. 2015; Bouwens et al. 2017; see also Dayal & Ferrara 2018 for a compilation of size evolution studies). Over the past decades, deep survey data of *HST* have allowed to uncover a variety of the morphological nature not only for such relatively massive populations, but also for a typically low-mass sys-

tem of Ly α emitters (LAEs; e.g., Venemans et al. 2005; Pirzkal et al. 2007; Overzier et al. 2008; Bond et al. 2009; Taniguchi et al. 2009; Gronwall et al. 2011; Malhotra et al. 2012; Bond et al. 2012; Jiang et al. 2013; Hayes et al. 2014; Shibuya et al. 2014a; Guaita et al. 2015; Hagen et al. 2016; Kobayashi et al. 2016; Wisotzki et al. 2016; Leclercq et al. 2017; Shimakawa et al. 2017; Yang et al. 2017a; Paulino-Afonso et al. 2018).

Some of the previous studies have quantified the radial SB profiles of the stellar continuum emission for LAEs with the Sérsic index (Sérsic 1963, 1968) to be $n \simeq 1$ at $z \simeq 3.1$ (Gronwall et al. 2011) and $z \simeq 5.7$ (Taniguchi et al. 2009). The results of the low n values suggest that LAEs have a disk-like SB profile. Recently, Paulino-Afonso et al. (2018) have shown that LAEs have a nearly constant Sérsic index of $n \lesssim 2$ at $z \simeq 2 - 6$ with a large sample of $\simeq 3000$ LAEs, indicating that the disk-like SB profile of LAEs does not significantly change over the cosmic time. In addition to the constraints on n , the radial SB profiles are useful for investigating the origins of extended Ly α emission, so-called Ly α halos, surrounding high- z star-forming galaxies (e.g., Hayashino et al. 2004; Rauch et al. 2008; Steidel et al. 2011; Matsuda et al. 2012; Momose et al. 2014, 2016; Matthee et al. 2016; Wisotzki et al. 2016; Sobral et al. 2017b; Xue et al. 2017; Leclercq et al. 2017). The diffuse and extended emission of the Ly α halos is expected to result from e.g., cold streams accreted onto the central galaxies, resonantly scattered Ly α radiation produced by star formation activities of neighboring small satellite galaxies, and/or the fluorescent Ly α emission created by the ionizing photons from the central sources (see recent review papers, e.g., Di-

Electronic address: tshibuya_@mail.kitami-it.ac.jp

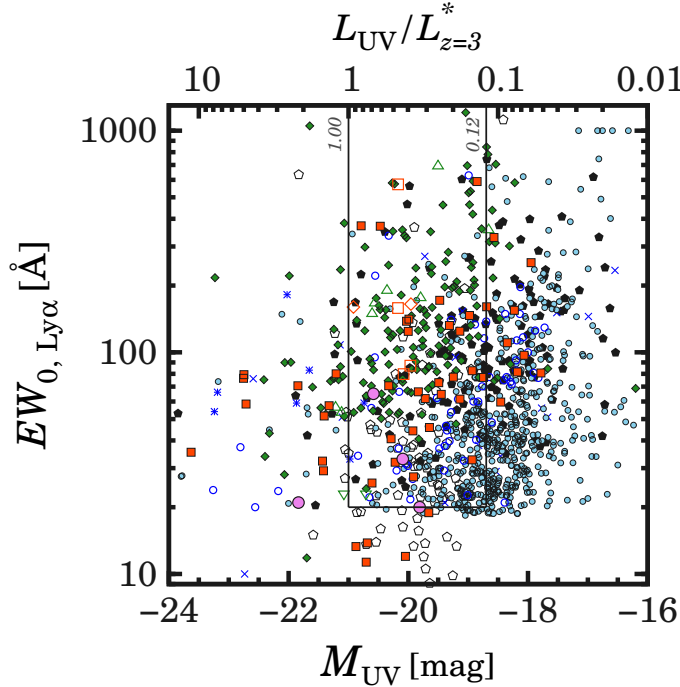
¹Kitami Institute of Technology, 165 Koen-cho, Kitami, Hokkaido 090-8507, Japan

²Institute for Cosmic Ray Research, The University of Tokyo, 5-1-5 Kashiwanoha, Kashiwa, Chiba 277-8582, Japan

³Kavli Institute for the Physics and Mathematics of the Universe (Kavli IPMU, WPI), University of Tokyo, Kashiwa, Chiba 277-8583, Japan

⁴Department of Physics, Graduate School of Science, The University of Tokyo, 7-3-1 Hongo, Bunkyo, Tokyo, 113-0033, Japan

⁵National Astronomical Observatory of Japan, 2-21-1 Osawa, Mitaka, Tokyo 181-8588, Japan



- | | | |
|-----------------------|--------------------------|--------------------------------|
| × Woll17 $z \sim 0.3$ | ◆ Sob17 $z \sim 3-6$ | ■ Ouc08,10 $z \sim 3.1-6.6$ |
| * Woll14 $z \sim 1$ | △ Fin09 $z \sim 4.5$ | □ Hu10 $z \sim 5.7-6.6$ |
| ○ Nak12 $z \sim 2.2$ | ▽ Shio09 $z \sim 4.9$ | ◇ Mat15 $z \sim 6.6$ |
| ○ Cia12 $z \sim 3.1$ | ● Lec17 $z \sim 2.9-6.6$ | ○ Car18 $z \sim 2.9-6.6$ |
| | | ○ I18,P18,O12,O15 $z \sim 7-8$ |

FIG. 1.— Ly α EW as a function of UV magnitude for LAEs used in this study (blue crosses: Wold et al. 2017; blue asterisks: Wold et al. 2014; cyan filled circles: Nakajima et al. 2012; blue open circles: Ciardullo et al. 2012; green filled diamonds: Sobral et al. 2017a; green open triangles: Finkelstein et al. 2009; green open inverse-triangles: Shioya et al. 2009; red filled squares: Ouchi et al. 2008, 2010; red open squares: Hu et al. 2010; red open diamonds: Matthee et al. 2015; black filled pentagons: Leclercq et al. 2017; black open pentagons: Caruana et al. 2018; magenta filled circles: Itoh et al. 2018, Pentericci et al. 2018, Ono et al. 2012, and Oesch et al. 2015). The Ly α EW of Itoh et al. (2018)’s LAE is assumed to be $EW_{0, Ly\alpha} = 20 \text{ \AA}$. This diagram shows LAEs whose effective radius is obtained in our GALFIT measurements. The top x-axis provides the corresponding UV luminosity in units of $L_{z=3}^*$ (see Section 2). The vertical and horizontal lines denote the thresholds of UV luminosity (i.e., $L_{UV} = 0.12 - 1L_{z=3}^*$) and Ly α EW (i.e., $EW_{0, Ly\alpha} > 20 \text{ \AA}$), respectively, for our analysis.

jkstra 2017; Dayal & Ferrara 2018). The image stacking analysis of ground-based telescope data has detected the faint and diffuse Ly α emission down to $SB \simeq 10^{-32-(-33)} \text{ erg}^{-1} \text{ s}^{-1} \text{ cm}^{-2} \text{ Hz}^{-1}$. Complementary to the image stacking analysis, the *HST* high spatial resolution observations enable us to compare the radial SB profiles in Ly α and the stellar continuum radiation near the galaxy center. The central part of the stellar radial SB profiles would be used for modeling star formation budgets from small satellite galaxies as a function of angular distance.

On the other hand, measurements of galaxy sizes, defined as the effective radius, r_e , in the stellar continuum emission have shown that LAEs are compact and do not typically evolve at $r_e \simeq 1 \text{ kpc}$ in the redshift range of $z \simeq 2 - 6$ (Malhotra et al. 2012; Hagen et al. 2014; Paulino-Afonso et al. 2018). For example, Paulino-

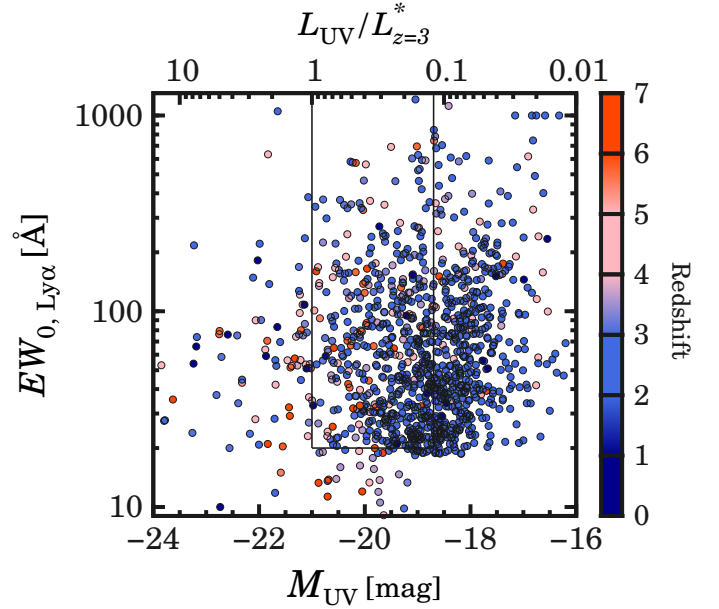


FIG. 2.— Same as Figure 1, but for LAEs that are color-coded based on the redshift.

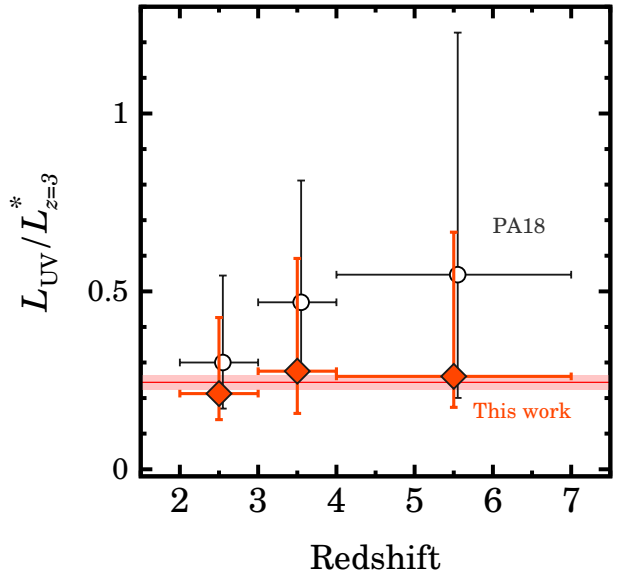


FIG. 3.— Median UV luminosity as a function of redshift for LAE samples of ours (red filled diamonds) and Paulino-Afonso et al. (2018)’s (open circles). The horizontal line and shaded region denotes the average L_{UV} value and its 1σ uncertainty of our median L_{UV} data points, respectively. The y-axis shows the UV luminosity in units of $L_{z=3}^*$. The error bars represent the 16th- and 84th-percentiles of the L_{UV} distribution.

Afonso et al. (2018) report that the median r_e scales as $r_e \propto (1+z)^{-0.21 \pm 0.22}$ at $z \simeq 2 - 6$ for LAEs, which is consistent with no size evolution scenario within a 1σ uncertainty. This is in contrast to the size evolution with $r_e \propto (1+z)^{-1 \sim -1.5}$ for other galaxy populations such as optical emission line galaxies (oELGs; e.g., Paulino-Afonso et al. 2017) and LBGs (e.g., Ferguson et al. 2004; Mosleh et al. 2012, 2013; Ono et al. 2013; Shibuya et al. 2015).

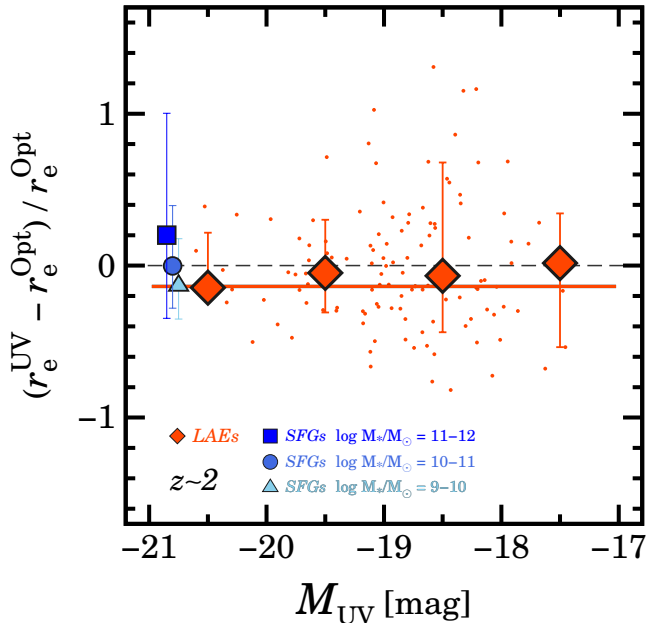


FIG. 4.— Difference between r_e^{UV} and r_e^{Opt} for the LAEs at $z \simeq 2.2$ (red dots) as a function of UV magnitude. The red diamonds with error bars represent the median values of $(r_e^{\text{UV}} - r_e^{\text{Opt}})/r_e^{\text{Opt}}$ in different M_{UV} bins. The horizontal line shows the average value of median $(r_e^{\text{UV}} - r_e^{\text{Opt}})/r_e^{\text{Opt}}$ data points. The blue symbols represent median values of $(r_e^{\text{UV}} - r_e^{\text{Opt}})/r_e^{\text{Opt}}$ for $z \simeq 2$ SFGs with $M_{\text{UV}} = -21 - (-20)$ in different stellar mass ranges (triangle: $\log M_*/M_\odot = 9 - 10$; circle: $\log M_*/M_\odot = 10 - 11$; square: $\log M_*/M_\odot = 11 - 12$; see Paper I). The data points are slightly shifted along the x -axis for clarity.

When considering the size evolution, it should be noted that the effective radius is strongly correlated with the galaxy luminosity (or galaxy mass) in the sense that a brighter source has a larger r_e . Galaxy sizes decrease with redshift following this *size-luminosity relation* (e.g., van der Wel et al. 2014; Shibuya et al. 2015). Contrary to expectations from the no size evolution of LAEs, several studies have reported that LAEs follow the evolving size-luminosity relation in samples of the Lyman alpha reference sample (LARS) project at $z \simeq 0$ (Guaita et al. 2015), integral field unit (IFU) surveys at $z \simeq 3 - 6$ (Leclercq et al. 2017; Wisotzki et al. 2016), narrow-band (NB) observations at $z \simeq 6 - 7$ (Jiang et al. 2016). These results are incompatible with the lack of size evolution in LAEs. Thus, there is a possibility that the no size evolution results for LAEs are originated from a bias caused by heterogeneous luminosity bins for a r_e comparison. To conclude whether the size evolution exists, we need to examine the size growth rate at a *given luminosity*. Recently, large LAE samples have been constructed by wide-field and deep surveys, as described in later sections. The combinations of the large LAE samples, the *HST* deep data, and a systematic analysis will allow us to study the morphological evolution for LAEs with no significant bias.

In this paper, we investigate the redshift evolution of the radial SB profile and the galaxy size with a sample of $\simeq 9,000$ LAEs at $z \simeq 0 - 8$ and the *HST* deep data of extra-galactic legacy surveys. This is the third paper in a

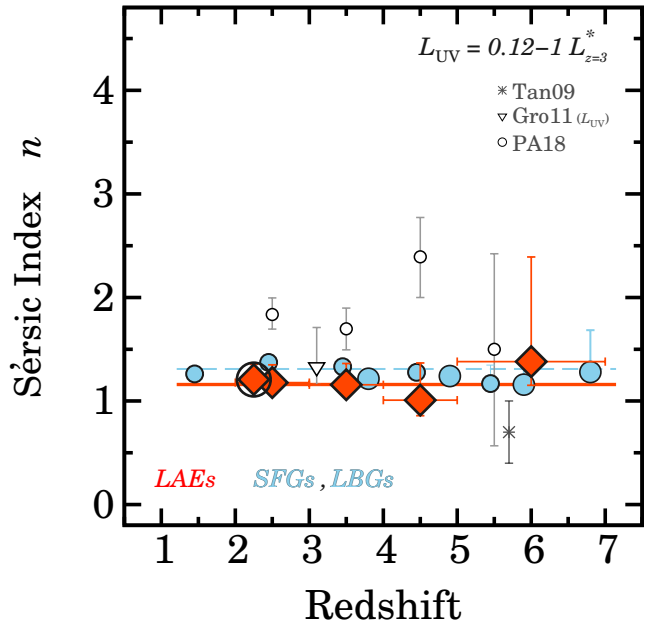


FIG. 5.— Sérsic index as a function of redshift in the UV luminosity bin of $L_{\text{UV}} = 0.12 - 1 L_{z=3}^*$. The red filled diamonds with and without an open circle represent the Sérsic index for LAEs in the rest-frame UV and optical continuum emission, respectively. The gray symbols indicate LAEs in previous studies (gray asterisks: Taniguchi et al. 2009; gray open circles: Paulino-Afonso et al. 2018; gray open inverse triangles: Gronwall et al. 2011). The measurement technique is noted in the parenthesis of the legend (S: SExtractor; G: GALFIT; see also Table 2). The median n value is calculated in the bin of $L_{\text{UV}} = 0.12 - 1 L_{z=3}^*$ for Gronwall et al. (2011) with n for individual sources, which is indicated as “ L_{UV} ” in the parenthesis of the legend. The small and large cyan filled circles denote the SFGs and LBGs, respectively (Paper I; see also Section 6.1). The magenta solid and cyan dashed horizontal line denote weighted means of $\langle n \rangle = 1.16$ for the LAEs and $\langle n \rangle = 1.31$ for the SFGs and LBGs, respectively. Our LAEs are not plotted at $z \lesssim 2$, because the number of LAEs with $L_{\text{UV}} = 0.12 - 1 L_{z=3}^*$ is too small. The data points are slightly shifted along the x -axis for clarity. The error bars of some data points are smaller than the size of symbols.

series studying the morphology of high- z galaxies.⁶ This paper is organized as follows. In Sections 2 and 3, we describe the details of our LAE sample and *HST* data, respectively. Section 4 presents methods to obtain radial SB profiles and r_e . In Section 5, we detail comparison samples of UV selected galaxies and LAEs in the literature. We present the redshift evolution of the radial SB profiles, the size-luminosity relation, r_e , and size-relevant physical quantities in Section 6. Section 7 discusses the implications for the galaxy formation and evolution. In Section 8, we summarize the findings in our study.

Throughout this paper, we adopt the concordance cosmology with $(\Omega_m, \Omega_\Lambda, h) = (0.3, 0.7, 0.7)$, (Planck Collaboration et al. 2016). All magnitudes are given in the AB system (Oke & Gunn 1983). We refer to the *HST* F606W, F775W, F814W, F850LP, F098M, F105W, F125W, F140W, and F160W filters as V_{606} , I_{814} , z_{850} , Y_{098} , Y_{105} , J_{125} , JH_{140} , and H_{160} , respectively.

⁶ The first and second papers examine galaxy sizes (Shibuya et al. 2015, hereafter Paper I) and clumpy structures (Shibuya et al. 2016, hereafter Paper II) using $\simeq 190,000$ galaxies at $z \simeq 0 - 10$, respectively.

TABLE 1
LAE SAMPLES USED FOR OUR SIZE MEASUREMENTS

Reference	z	N_{LAE}	$N_{\text{HST}}^{\text{UV}}$	$N_{\text{GALFIT}}^{\text{UV}}$	$N_{\text{HST}}^{\text{opt}}$	$N_{\text{GALFIT}}^{\text{opt}}$	$EW_{0,\text{Ly}\alpha}^{\text{limit}}$ [Å]	<i>HST</i> Field	Related Ref.
(1)	(2)	(3)	(4)	(5)	(6)	(7)	(8)	(9)	(10)
Wold et al. (2017)	0.3	173	—	—	18	13	—	cos, gds, aeg	Deh08, Cow10
Wold et al. (2014)	1	135	—	—	9	4	—	cos, gds, aeg	Cow11, Bar12
Nakajima et al. (2012)	2.2	3373	591	323	503	268	> 20 – 30	cos, uds, gds, gdn	
Ciardullo et al. (2012)	3.1	199	56	32	—	—	> 20	gds	Gro07
Sobral et al. (2017a)	3.1	45	8	4	—	—	> 25	cos	
	2.4 – 2.6 ^b	741	43	30	—	—	> 50	cos	
	2.7 – 2.9 ^b	311	9	8	—	—	> 50	cos	
	2.9 – 3.1 ^b	711	41	21	—	—	> 50	cos	
	3.1 – 3.3 ^b	483	26	17	—	—	> 50	cos	
	3.2 – 3.4 ^b	641	26	8	—	—	> 50	cos	
	3.6 – 3.9 ^b	98	2	0	—	—	> 50	cos	
	4.0 – 4.3 ^b	142	6	0	—	—	> 50	cos	
	4.4 – 4.7 ^b	79	4	2	—	—	> 50	cos	
	4.7 – 5.0 ^b	81	6	3	—	—	> 50	cos	
	4.9 – 5.2 ^b	79	3	1	—	—	> 50	cos	
	5.2 – 5.5 ^b	33	1	0	—	—	> 50	cos	
	5.6 – 5.9 ^b	35	0	0	—	—	> 50	cos	
Finkelstein et al. (2009)	4.5	14	14	7	—	—	\gtrsim 50	gds	
Shioya et al. (2009)	4.9	79	2	1	—	—	> 11	cos	
Ouchi et al. (2008)	3.1	356	15	1	—	—	\gtrsim 64	uds	
	3.7	101	7	2	—	—	\gtrsim 44	uds	
	5.7	401	18	5	—	—	\gtrsim 27	uds	
Murayama et al. (2007)	5.7	119	4	0	—	—	> 18	cos	
Hu et al. (2010)	5.7	88	4	0	—	—	—	gdn	
	6.5	30	0	0	—	—	—	gdn	
Ouchi et al. (2010)	6.6	207	14	5	—	—	\gtrsim 14	uds	
Matthee et al. (2015)	6.6	16	2	1	—	—	\gtrsim 38	cos	
Leclercq et al. (2017) ^a	2.9 – 6.6	184	180	97	—	—	\gtrsim 20	hudf	
Caruana et al. (2018) ^a	2.9 – 6.6	100	100	78	—	—	—	gds	Her17
Itoh et al. (2018)	7	34	4	1	—	—	\gtrsim 10	cos, uds	Ino
Ota et al. (2017)	7	20	2	1 ^c	—	—	> 10	uds	
Hu et al. (2017)	7	6	0	0	—	—	> 10	cos	Zhe17
Pentericci et al. (2018) ^d	7	2	2	1	—	—	—	cos, uds, gds	
Shibuya et al. (2012)	7.2	1	0	0	—	—	—	uds	
Ono et al. (2012)	7.2	1	1	1	—	—	—	gdn	Ouc09
Oesch et al. (2015)	7.7	1	1	1	—	—	—	aeg	Smi15
Total	—	9119	1192	651	530	285	—	—	—

NOTE. — Columns: (1) Reference. (2) Redshift range of the LAE sample. (3) Number of LAEs in the sample. (4) Number of LAEs whose rest-frame UV continuum emission is covered by a passband of the *HST* images. (5) Number of LAEs whose r_e^{UV} value is obtained in our size measurements. (6) Number of LAEs whose rest-frame optical continuum emission is covered by a passband of the *HST* images. (7) Number of LAEs whose r_e^{opt} value is obtained in our size measurements. (8) Typical Ly α EW limit of the LAE survey. (9) *HST* field (“gds”: GOODS-South; “gdn”: GOODS-North; “uds”: UDS; “aeg”: AEGIS; “cos”: COSMOS; “hudf”: Hubble Ultra Deep Field). (10) Reference related to the LAE sample (“Deh08”: Deharveng et al. 2008; “Cow10”: Cowie et al. 2010; “Cow11”: Cowie et al. 2011; “Bar12”: Barger et al. 2012; “Gro07”: Gronwall et al. 2007; “Her17”: Herenz et al. 2017; “Ino”: A. K. Inoue et al. in preparation; “Zhe17”: Zheng et al. 2017; “Ouc09”: Ouchi et al. 2009; “Smi15”: Smit et al. 2015)

^a IFU observations.

^b MB filter observations.

^c This object is identical to a $z \simeq 7$ LAE selected by Itoh et al. (2018).

^d Only the galaxies at $z > 7$ are selected.

2. LAE SAMPLE

To perform a statistical study on galaxy structures, we construct a large LAE sample by combining several catalogs of LAEs at $z \simeq 0 - 8$ in the literature: LAEs obtained from *GALEX* space-based spectroscopy (Wold et al. 2017, 2014), ground-based NB and medium-band (MB) imaging (Nakajima et al. 2012; Ciardullo et al. 2012; Sobral et al. 2017a; Finkelstein et al. 2009; Shioya et al. 2009; Ouchi et al. 2008; Murayama et al. 2007; Hu et al. 2010; Ouchi et al. 2010; Matthee et al. 2015; Itoh et al. 2018; Ota et al. 2017), IFU observations with the Multi Unit Spectroscopic Explorer (MUSE; Bacon et al. 2010) on the Very Large Telescope (Leclercq et al. 2017; Caruana et al. 2018), and spectroscopic observations for

$z \simeq 7 - 8$ (Hu et al. 2017; Pentericci et al. 2018; Ono et al. 2012; Shibuya et al. 2012; Oesch et al. 2015). The $z \simeq 7 - 8$ LAEs are not used, but for a $z-r_e$ diagram, because of the small statistics. The sample contains 9119 LAEs in total. Table 1 lists the redshift range and the object number of each LAE catalog. Figure 1 shows the absolute UV magnitude, M_{UV} , and the rest-frame Ly α equivalent width (EW), $EW_{0,\text{Ly}\alpha}$. Thanks to the combination of space-based spectroscopic, ground-based imaging and IFU data, the LAE sample covers wide ranges of M_{UV} and $EW_{0,\text{Ly}\alpha}$.

We find some features of the heterogeneity in M_{UV} and $EW_{0,\text{Ly}\alpha}$ between low- z and high- z samples. For example, as clearly shown at $M_{\text{UV}} \simeq -18 - (-16)$ in Figure 1,

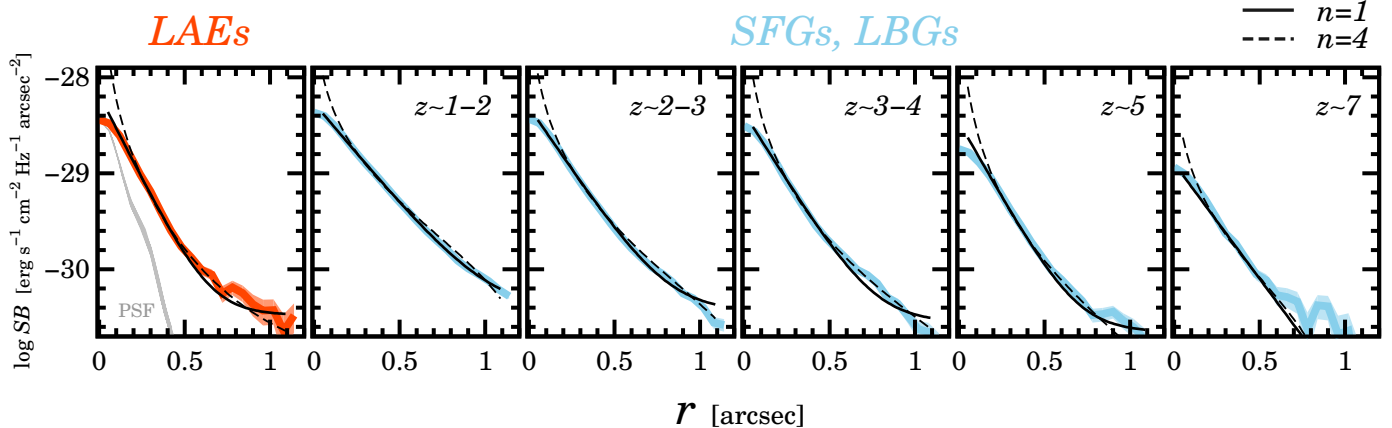


FIG. 6.— Radial SB profiles at λ_{UV} for LAEs (red), SFGs, and LBGs (cyan) in the UV luminosity bin of $L_{UV} = 0.12 - 1L_{z=3}^*$. The panels, from left to right, indicate the LAEs at $z \simeq 0 - 7$, SFGs at $z = 1 - 2$, $z = 2 - 3$, $z = 3 - 4$, LBGs at $z \simeq 5$, and $z \simeq 7$. The shaded regions show the 1σ uncertainty of the radial SB profiles. The solid and dashed black curves depict the best-fit Sérsic profiles with $n = 1$ and $n = 4$, respectively. The gray line shows a typical PSF of the H_{160} image.

faint sources tend to be preferentially selected at low- z . See also Figure 2 which is the same as Figure 1, but for color-coded symbols based on the redshift. To avoid this selection effect, we apply a UV luminosity bin of $0.12 - 1 L_{UV}/L_{z=3}^*$, where $L_{z=3}^*$ is the characteristic UV luminosity of LBGs at $z \sim 3$ ($M_{UV} = -21$, Steidel et al. 1999). To exclude several objects with a relatively low $Ly\alpha$ EW, we also select LAEs with $EW_{0, Ly\alpha} > 20\text{\AA}$ which is the well-used $EW_{0, Ly\alpha}$ criterion for LAE surveys.

In Figure 3, we check whether there is no significant difference in typical L_{UV} values in the redshift range. Our LAE sample shows a nearly constant L_{UV} value of $L_{UV}/L_{z=3}^* \simeq 0.25$. We also plot the median L_{UV} of Paulino-Afonso et al. (2018) which is the most recent statistical study on the LAE size evolution. In contrast to our LAE sample, Paulino-Afonso et al. (2018)’s L_{UV} values increase from $L_{UV}/L_{z=3}^* \simeq 0.25$ at $z = 2 - 3$ to $L_{UV}/L_{z=3}^* \simeq 0.5$ at $z = 4 - 7$. Section 7.1 discusses the importance of the L_{UV} cut on the galaxy size evolution.

3. HST DATA

We make use of deep *HST* imaging data taken by the Cosmic Assembly Near-infrared Deep Extragalactic Legacy Survey (CANDELS; Grogin et al. 2011; Koekoemoer et al. 2011). The CANDELS consists of five deep fields, GOODS-South, GOODS-North, UDS, AEGIS, and COSMOS. These *HST* images are retrieved from the website of the 3D-HST project (Skelton et al. 2014).⁷ We also use the *Hubble* Ultra Deep Field 09+12 (HUDF 09+12; Beckwith et al. 2006; Bouwens et al. 2011; Illingworth et al. 2013; Ellis et al. 2013)⁸ to examine LAEs in the MUSE deep field (Leclercq et al. 2017).

The typical 5σ limiting magnitudes in a $0''.35$ diameter aperture are $\simeq 28 - 29$ mag for CANDELS and $\simeq 30$ mag for HUDF 09+12. The full width half maximum (FWHM) of the point spread function (PSF) are $\simeq 0''.08 - 0''.09$ and $\simeq 0''.12 - 0''.18$ in the Advanced Camera for Surveys (ACS) and Wide Fields Camera 3 (WFC3)/IR images, respectively. The full set of the limiting magnitudes and PSF FWHM is provided in Table

1 of Paper I.

4. ANALYSIS

Using the *HST* images, we measure the structural quantities for individual sources of the LAE sample. The method of the analysis is the same as that in Paper I, but is briefly described here. First, we extract $18'' \times 18''$ cutout images from the *HST* data at the position of each LAE. Next, we obtain structural quantities such the half-light radius along the semi-major axis, $R_{e, \text{major}}$, the Sérsic index, n , and the position angle (P.A.), the axial ratio, q , by performing the two-dimensional (2D) Sérsic profile (Sérsic 1963, 1968) fitting with the GALFIT software (Peng et al. 2002, 2010). The $R_{e, \text{major}}$ is converted to the “circularized” radius, r_e , through $r_e \equiv R_{e, \text{major}} \sqrt{q}$. In the GALFIT fitting, we input the *sigma*, *mask*, and PSF images. The *sigma* and *mask* images are used for the fitting weight of individual pixels and masking neighboring objects of the main galaxy components, respectively. The mask images also remove the light of galaxy clumpy structures, enabling us to focus on analyses for the main galaxy components. The PSF images of each *HST* field are provided in the 3D-HST project (Skelton et al. 2014). The ranges of the structural parameters varying in the fitting are $\Delta m < 3$ mag, $0.3 < R_{e, \text{major}} < 400$ pixels, $0.2 < n < 8$, $0.0001 < q < 1$, $\Delta x < 4$ pixel, and $\Delta y < 4$ pixel, where m and (x, y) are the magnitude and the coordinates in the *HST* images. The objects are discarded if one or more fitting parameters reach the limit of the parameter ranges (e.g., $R_{e, \text{major}} = 400$ pixel). The cosmological SB dimming would not significantly affect our measurements of structural quantities, at least at $M_{UV} \lesssim -18$, which has been evaluated in Paper I. To avoid a possible profile fitting degeneracy between r_e and m obtained in GALFIT, we employ MAG_AUTO derived with SExtractor as a total magnitude. See Paper I for more details of our analysis.⁹

To minimize the effect of morphological K -correction for LAEs at different redshifts of $z \simeq 0 - 8$, we utilize

⁷ <http://3dhst.research.yale.edu/Home.html>

⁸ <http://archive.stsci.edu/prepds/xd/>

⁹ Some recent studies have performed a sophisticated technique to simultaneously determine the size-luminosity relation and the UV luminosity functions (e.g., Kawamata et al. 2018).

TABLE 2
STATISTICAL STUDIES ON LAE SIZES IN THE LITERATURE

Reference (1)	$N_{\text{GALFIT}}(N_{\text{LAE}})$ (2)	z (3)	Size Measurements (4)	LAE Catalog (5)
Guaita et al. (2015)	14 (14)	0.1	SExtractor, PHOT, ELLIPSE	Östlin et al. (2014)
Yang et al. (2017a)	24 (43)	0.1 – 0.3	FWHM	Yang et al. (2017b)
Hagen et al. (2016)	28 (28)	2	PHOT	compilation
Shibuya et al. (2014a)	663 (1239)	2.2	SExtractor	Nakajima et al. (2012)
Bond et al. (2009)	... (120)	3.1	PHOT	Gronwall et al. (2007)
Gronwall et al. (2011)	78 (78)	3.1	GALFIT	Gronwall et al. (2007)
Hagen et al. (2014)	63 (99)	1.9 – 3.6	PHOT	Blanc et al. (2011)
Shimakawa et al. (2017)	50 (50)	2.5	GALAPAGOS	Shimakawa et al. (2017)
Bond et al. (2012)	... (108)	2.1	PHOT	Gronwall et al. (2007)
	... (171)	3.1	PHOT	Ciardullo et al. (2012)
Kobayashi et al. (2016)	54 (61)	4.9	SExtractor	Shioya et al. (2009)
Taniguchi et al. (2009)	47 (119)	5.7	SExtractor	Murayama et al. (2007)
Malhotra et al. (2012)	174 (174)	2.35 – 6	compilation	compilation
Pirzkal et al. (2007)	... (9)	4 – 5.7	GALFIT	Xu et al. (2007)
Jiang et al. (2013)	... (51)	5.7 – 7	SExtractor	compilation
Wisotzki et al. (2016)	... (26)	2.9 – 6.6	exponential fit	Bacon et al. (2015)
Leclercq et al. (2017)	... (145)	2.9 – 6.6	exponential fit	Bacon et al. (2017)
Paulino-Afonso et al. (2018)	429 (3045)	2 – 6	GALFIT	compilation
This work	936 (9119)	0.3 – 7.7	GALFIT	compilation

NOTE. — Columns: (1) Reference. (2) Number of galaxies whose effective radius is measured in the reference. The values in parentheses are the number of galaxies in the parent sample. (3) Redshift range for size measurements of LAEs. (4) Method or software to measure galaxy sizes. See the text in Section 5. (5) Reference of LAE catalog used for the size measurements. The “compilation” indicates that the study uses an LAE sample compiled from several LAE catalogs.

several bands of images taken with ACS and WFC3/IR on *HST*. Based on the redshift of LAEs, we select a pass-band from V_{606} , I_{814} , J_{125} , H_{160} , or the coadd WFC3 band for covering the wavelength ranges of the rest-frame UV, $\lambda_{\text{UV}} \simeq 1500 - 3000 \text{ \AA}$, or the rest-frame optical, $\lambda_{\text{Opt}} \simeq 4500 - 8000 \text{ \AA}$, emission. The effective radius measured in λ_{UV} and λ_{Opt} are referred to as r_e^{UV} and r_e^{Opt} , respectively. In *HST* fields where the Y_{105} band is available (i.e., HUDF 09+12, GOODS-South, and GOODS-North), we use coadded images constructed from four or five WFC3/IR bands (Harikane et al. 2016).

Table 1 summarizes the numbers of LAEs that are covered by the *HST* images and are well fitted by GALFIT. The total numbers of LAEs whose structural quantities are obtained in λ_{UV} and λ_{Opt} are 651 and 285, respectively. We have excluded candidates of active galactic nuclei by checking X-ray and radio wavelength source catalogs of e.g., the *XMM-Newton* 0.2 – 10.0 keV band and Very Large Array 1.4 GHz (see Nakajima et al. 2012; Konno et al. 2016 for more details).

Here we compare r_e^{UV} and r_e^{Opt} of the LAEs at $z \simeq 2.2$ where both the radii can be obtained with the *HST* data. Figure 4 shows the differences between r_e^{UV} and r_e^{Opt} as a function of M_{UV} . Albeit with a large scatter, the median values of $(r_e^{\text{UV}} - r_e^{\text{Opt}})/r_e^{\text{Opt}}$ are $\lesssim 20\%$ in all the M_{UV} bins. This indicates that the effect of morphological K -correction are small for LAEs at $z \simeq 2.2$. Although r_e^{UV} agrees well with r_e^{Opt} , the two radii are analyzed independently for measurements of e.g., the size growth rate, in the following sections. The r_e^{Opt} data points are used just for a reference.

For comparison, we plot $z \simeq 2$ SFGs of Paper I in Figure 4. In Paper I, we have found that r_e^{UV} relative to r_e^{Opt} is larger for more massive SFGs in a stellar mass range of $\log M_*/M_\odot \simeq 9 - 12$. This trend could be interpreted as large dust attenuation in the galactic central regions (e.g., Kelvin et al. 2012) and/or the inside-out

disk formation (e.g., Bezanson et al. 2009; Brooks et al. 2009) for massive SFGs. Similar to the low mass SFGs with $\log M_*/M_\odot \simeq 9 - 10$, our LAEs show, on average, a small r_e^{UV} relative to r_e^{Opt} . According to an $M_{\text{UV}} - M_*$ empirical relation in Paper I, the stellar mass for our LAEs corresponds to $\log M_*/M_\odot \simeq 9 - 10$ that is comparable to M_* for the low mass SFGs. Thus, the consistency in $r_e^{\text{UV}}/r_e^{\text{Opt}}$ and M_* might suggest that LAEs typically have small amounts of dust at the galactic central regions and/or have not experienced the inside-out disk formation.

5. COMPARISON SAMPLES

To make a comparison in structural properties between LAEs and other galaxy populations, we use 165517 photo- z SFGs at $z = 0 - 6$ in Skelton et al. (2014) and 10454 LBGs at $z \simeq 4 - 10$ in Harikane et al. (2016). The n and r_e values for these SFGs and LBGs are measured in Paper I in the same method as those for LAEs (Section 4). This ensures a fair comparison in the structural quantities. In Paper I, the Sérsic index has not been obtained for the LBGs because the n parameter is fixed for a fair comparison with previous studies on LBGs. In this study, we calculate the Sérsic index for the LBGs to compare with LAEs at a high redshift of $z \simeq 6 - 7$.

We also use the n and r_e measurements for LAEs in individual previous studies of Guaita et al. (2015), Hagen et al. (2016), Gronwall et al. (2011), Bond et al. (2012), Kobayashi et al. (2016), Taniguchi et al. (2009), Malhotra et al. (2012), Jiang et al. (2013), Paulino-Afonso et al. (2018). Table 2 summarizes the redshift range, the number of LAEs, and the method to measure structural quantities for these references including statistical studies on the galaxy morphology (i.e., Pirzkal et al. 2007; Shibuya et al. 2014a; Hagen et al. 2014; Wisotzki et al. 2016; Yang et al. 2017a; Shimakawa et al. 2017; Leclercq et al. 2017). The effective radius is derived in different techniques or softwares such as GALFIT, GALAPAGOS (Bar-

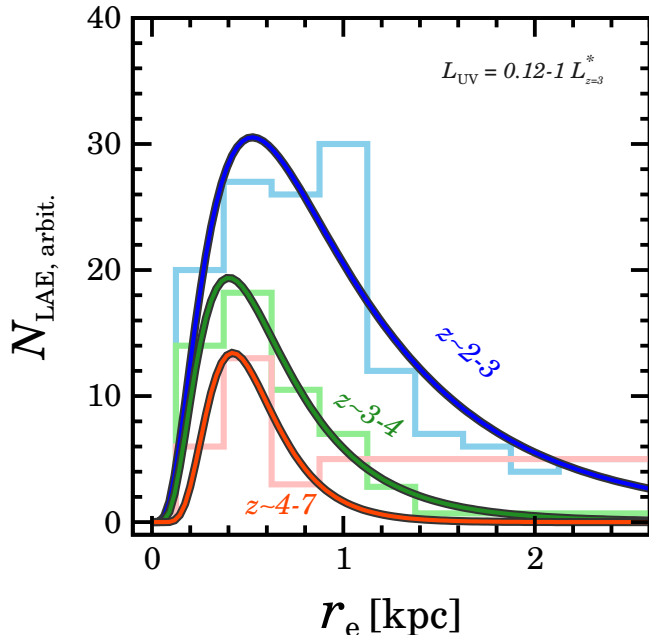


FIG. 7.— Distribution of r_e^{UV} for the LAEs in the UV luminosity bin of $L_{\text{UV}} = 0.12 - 1 L_{z=3}^*$. The histograms and the curves show the r_e^{UV} distributions and the best-fit log-normal functions, respectively, for the LAEs at $z \simeq 2 - 3$ (blue), $z \simeq 3 - 4$ (green), and $z \simeq 4 - 7$ (red). The y-axis is arbitrary.

TABLE 3
SIZE-LUMINOSITY RELATION FOR LAES

M_{UV} [mag]	r_e^{Opt} [kpc]	M_{UV} [mag]	r_e^{UV} [kpc]	M_{UV} [mag]	r_e^{UV} [kpc]
(1)	(2)	(3)	(4)	(5)	(6)
$z = 0 - 1$		$z \simeq 2$		$z \simeq 4$	
-19.0	$1.44^{+0.148}_{-0.155}$	-20.0	$0.990^{+0.102}_{-0.042}$	-20.0	$0.546^{+0.065}_{-0.041}$
-17.0	$1.02^{+0.508}_{-0.152}$	-18.0	$0.925^{+0.065}_{-0.030}$	-18.0	$0.481^{+0.072}_{-0.043}$
$z \simeq 2$		$z \simeq 3$		$z \simeq 5$	
-20.0	$1.11^{+0.092}_{-0.062}$	-20.0	$0.705^{+0.081}_{-0.065}$	-21.0	$0.505^{+0.369}_{-0.044}$
-18.0	$0.938^{+0.073}_{-0.040}$	-18.0	$0.387^{+0.104}_{-0.036}$	-19.0	$0.466^{+0.042}_{-0.035}$
...		$z \simeq 6$
...	-22.0	$0.785^{+0.221}_{-0.221}$
...	-20.0	$0.543^{+1.64}_{-0.203}$

NOTE. — Columns: (1) (3) (5) UV magnitude. (2) (4) (6) Median effective radius and its standard error at the rest-frame optical or UV wavelengths.

den et al. 2012), SExtractor (Bertin & Arnouts 1996), or PHOT/ELLIPSE in IRAF, noted in a column of Table 2. Among the previous studies, Guaita et al. (2015), Hagen et al. (2016), Bond et al. (2012), Gronwall et al. (2011), Taniguchi et al. (2009), and Kobayashi et al. (2016) provide the structural quantities of n and r_e with M_{UV} for individual sources in readable tables. Using the tables, we re-calculate representative values of n and r_e in the M_{UV} bins.

6. RESULTS

We present results of our structure analyses: the Sérsic index (Section 6.1), the r_e distribution (Section 6.2), the size-luminosity relation (Section 6.3), the size evolution (Section 6.4), and the star formation rate surface den-

sity (SFR SD; Section 6.5). Similar to Paper I, results are shown in a UV luminosity bin of $0.12 - 1 L_{\text{UV}}/L_{z=3}^*$. For the representative values and uncertainties of these structural quantities, we employ the medians and standard errors, respectively, unless otherwise specified. For the previous studies on LAEs, we re-calculate the medians and standard errors if structural quantities of individual sources are available (see Section 5).

6.1. Sérsic Index

The left panel of Figure 6 shows the Sérsic index as a function of redshift. We find that LAEs have a nearly constant n value of $n \simeq 1 - 1.5$ in a wide redshift range of $z \simeq 2 - 7$. There is no significant difference in n for LAEs at $z \simeq 2$ between the rest-frame UV and optical wavelengths. This constant and low n value is comparable to the n trend for the SFGs and LBGs. The n result in our LAE sample are consistent with that in previous studies on LAEs, Taniguchi et al. (2009) and Gronwall et al. (2011). Paulino-Afonso et al. (2018)'s Sérsic index is slightly higher than our and these previous studies' results by $\Delta n \simeq 0.5 - 1$, but is still lower than $n \simeq 2 - 3$. We confirm that LAEs show no significant evolution in Sérsic index and a low n value of $n \simeq 1 - 1.5$, previously reported in Paulino-Afonso et al. (2018). This low Sérsic index indicates that LAEs typically have a disk-like SB profile in the stellar continuum emission.

Complementary to the n measurements for the individual sources, we also investigate the radial SB profiles in the stacked galaxy images. In Figure 6, we demonstrate that the radial SB profiles are similar to the exponential function (i.e., $n = 1$) instead of de Vaucouleurs' law (i.e., $n = 4$). The stacked galaxy images are created in a method similar to that in Paper II. We fit the 1D Sérsic functions with $n = 1$ and $n = 4$ to the radial SB profiles. The data points at $r > 0.2$ arcsec are used for the fitting to avoid the PSF broadening effect (Paper II). As shown at the galactic central regions of $r < 0.2$ arcsec, the 1D Sérsic function with $n = 4$ deviates from the radial SB profiles of the LAEs, SFGs, and LBGs. Based on the fitting results at the high- S/N central regions, we conclude that our SB profiles are better represented by the function of $n = 1$ than $n = 4$. The analysis of the stacked *HST* images supports the measurements of $n \simeq 1$ for individual LAEs. These radial SB profiles in the stacked *HST* images are analyzed for a comparison with Ly α halos in Section 7.3.

6.2. Distribution of the effective radius

We investigate the distribution of the effective radius, r_e , and its width. According to the galaxy disk formation models of e.g., Fall & Efstathiou (1980), Barnes & Efstathiou (1987), Warren et al. (1992), Mo et al. (1998), Bullock et al. (2001) and results of DM N-body simulations, the DM spin parameter λ is predicted to have a log-normal distribution with the standard deviation of $\sigma_{\ln \lambda} \sim 0.5 - 0.6$. If the stellar components of LAEs form in such disk formation mechanisms and r_e is determined by λ , the r_e distribution should be log-normal and $\sigma_{\ln r_e} \simeq 0.5 - 0.6$ similar to λ . Recently, the disk formation models have been tested with observational r_e data of galaxies at $z \simeq 0 - 3$ (e.g., Hearin et al. 2017; Huang et al. 2017; Okamura et al. 2018; Somerville et al. 2018; Fall & Romanowsky 2018).

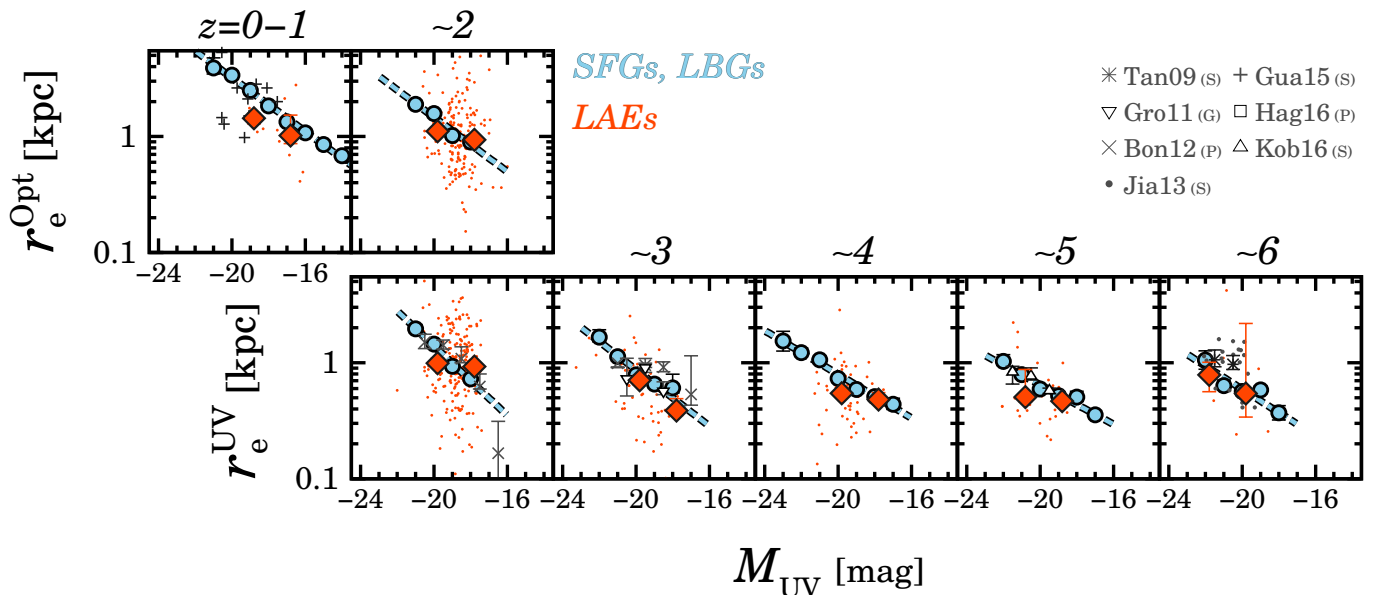


FIG. 8.— Effective radius, r_e and UV magnitude M_{UV} relation. The top and bottom panels represent r_e^{Opt} and r_e^{UV} , respectively. The redshifts are labeled at the top of the panels. The red filled diamonds and dots indicate the representative and individual r_e measurements for the LAEs. The cyan filled circles represent the SFGs and LBGs (Paper I). The cyan dashed lines denote the best-fit power-law functions of $r_e \propto L_{UV}^\alpha$ for the r_e - M_{UV} relations. The gray symbols present LAEs in the literature (gray asterisks: Taniguchi et al. 2009; gray open inverse triangles: Gronwall et al. 2011; gray x-marks: Bond et al. 2012; gray dots: Jiang et al. 2013; gray crosses: Guaita et al. 2015; gray open squares: Hagen et al. 2016; gray open triangles: Kobayashi et al. 2016). The measurement technique is noted in the parenthesis of the legend (S: SExtractor; G: GALFIT; P: PHOT; see also Table 2). The data points are slightly shifted along the x -axis for clarity. The error bars of some data points are smaller than the size of symbols.

Figure 7 presents the r_e^{UV} distribution of our LAEs in $L_{UV} = 0.12 - 1 L_{z=3}^*$. The LAEs appear to be represented by a log-normal distribution albeit with poor statistics especially for $z \simeq 4 - 7$. The r_e distribution is fitted by the log-normal function of

$$p(r_e) = \frac{1}{r_e \sigma_{\ln r_e} \sqrt{2\pi}} \exp\left[-\frac{\ln^2(r_e/\bar{r}_e)}{2\sigma_{\ln r_e}^2}\right] \quad (1)$$

where \bar{r}_e and $\sigma_{\ln r_e}$ are the peak of r_e and the standard deviation of $\ln r_e$, respectively. We obtain the best-fit distribution width of $\sigma_{\ln r_e} = 0.72 \pm 0.06$ at $z \simeq 2 - 3$, 0.59 ± 0.02 at $z \simeq 3 - 4$, and 0.42 ± 0.10 at $z \simeq 4 - 7$ corrected for the uncertainty of r_e measurements. These $\sigma_{\ln r_e}$ values are comparable to $\sigma_{\ln r_e} \simeq 0.45 - 0.75$ of the SFGs and LBGs estimated in Paper I and the width of the DM spin parameter, $\sigma_{\ln r_e} \simeq 0.5 - 0.6$. This result might imply that the stellar components of LAEs form in the galaxy disk formation models. The relation between the galaxy formation and the LAE morphology is discussed in Section 7.2 in details.

6.3. Size-Luminosity Relation

We explore the size-luminosity, r_e - L_{UV} , relation. Figure 8 shows the r_e - L_{UV} relation for the LAEs, SFGs, and LBGs, where L_{UV} is presented with the corresponding M_{UV} . We find a trend that r_e is larger at a brighter L_{UV} (i.e., smaller M_{UV}) for the LAEs, similar to the SFGs and LBGs. Although the some median r_e slightly deviate from the r_e - L_{UV} relation of the SFGs and LBGs (e.g., at $z \simeq 5$), the data points for the LAEs are consistent with those of the SFGs and LBGs within a 1σ error. This trend is shown in both of the rest-frame UV and optical wavelengths (i.e., the top and bottom panels

in Figure 8). Figure 8 also provides the best-fit r_e - L_{UV} relation obtained in Paper I for the SFGs and LBGs:

$$r_e = r_0 \left(\frac{L_{UV}}{L_0}\right)^\alpha, \quad (2)$$

where r_0 and α are free parameters. The L_0 values are employed as the typical UV luminosity at $M_{UV} = -21$. Our LAEs approximately follow the best-fit r_e - L_{UV} relation of the SFGs and LBGs. Each r_e value of the LAEs is listed in Table 3.

We compare our measurements with that of previous studies on LAEs, Taniguchi et al. (2009), Gronwall et al. (2011), Bond et al. (2012), Jiang et al. (2013), Guaita et al. (2015), Hagen et al. (2016), and Kobayashi et al. (2016). Similar to our LAE sample, LAEs in these previous studies are located around the r_e - L_{UV} relation of the SFGs and LBGs.

6.4. Size Evolution

We examine the redshift evolution in galaxy sizes. In this study, we discuss the evolutionary trend of median r_e which is a proxy for the typical galaxy size of our samples. Figure 9 plots the effective radius as a function of redshift for our LAE, SFG, and LBG samples. As shown in Figure 9, the LAEs significantly evolve in r_e at the rest-frame UV wavelength from $r_e^{\text{UV}} \simeq 0.5$ kpc at $z \simeq 4 - 6$ to $r_e^{\text{UV}} \simeq 1$ kpc at $z \simeq 2$, similarly found for the SFGs and LBGs. We parametrize the size growth rate by fitting a function of $r_e(z) = B(1+z)^\beta$, where B and β are free parameters. The fitting is performed using only the three r_e^{UV} values from $z \simeq 2$ to $z \simeq 7$. We find that r_e^{UV} scales as $\propto (1+z)^{-1.37 \pm 0.65}$, indicating that there

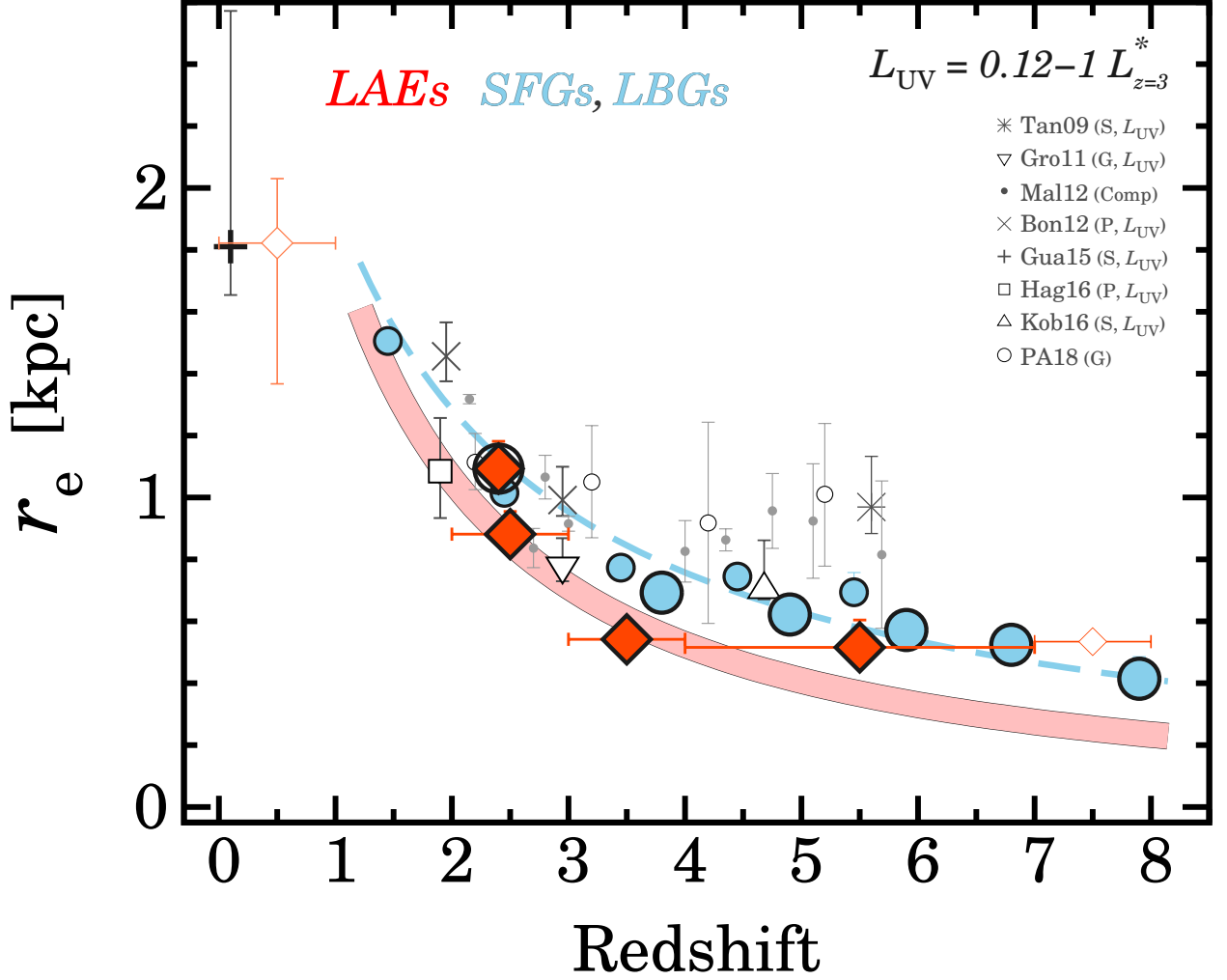


FIG. 9.— Redshift evolution of r_e in the L_{UV} range of $0.12 - 1 L_{z=3}^*$. The red filled diamonds with and without an open circle represent r_e^{UV} and r_e^{Opt} values measured for our LAEs, respectively. The red open diamond at $z \simeq 0 - 1$ is r_e^{Opt} for LAEs at $z \simeq 0 - 1$ which is inferred from the extrapolation of the size-luminosity relation in Figure 8 (see also Section 6.3 in more details). The red open diamond at $z \simeq 7.5$ represents r_e^{UV} measured from the three LAEs at $z \simeq 7 - 8$. The error bars of r_e^{UV} at $z \simeq 7 - 8$ are not reliably estimated because of the small statistics. The small and large cyan filled circles indicate the SFGs and LBGs, respectively (Paper I). The magenta solid and cyan dashed lines present the best-fit $(1+z)^\beta$ functions for the LAEs and SFGs/LBGs, respectively. The best-fit β value for r_e^{UV} of the LAEs is -1.37 ± 0.65 , which is obtained from the three r_e^{UV} data points at $z \simeq 2 - 7$. The gray symbols present LAEs in the literature (gray asterisks: Taniguchi et al. 2009; gray open inverse triangles: Gronwall et al. 2011; gray x-marks: Bond et al. 2012; gray dots: Malhotra et al. 2012; gray crosses: Guaita et al. 2015; gray open squares: Hagen et al. 2016; gray open triangles: Kobayashi et al. 2016; gray open circles: Paulino-Afonso et al. 2018). The measurement technique is noted in the parenthesis of the legend (S: SExtractor; G: GALFIT; P: PHOT; see also Table 2). Malhotra et al. (2012) compile several results of r_e measurements in the literature. For the previous studies with “ L_{UV} ” in the parenthesis of the legend, the median r_e value is calculated in the range of $L_{UV} = 0.12 - 1 L_{z=3}^*$. The data points are slightly shifted along the x -axis for clarity. The error bars of some data points are smaller than the size of symbols.

is a size evolution similar to the SFGs and LBGs with $\beta \simeq -1 \sim -1.5$ (Paper I). This result is consistent with the evolution of the size-luminosity relation for the LAEs, SFGs, and LBGs, as shown in Section 6.3. The galaxy size at the rest-frame optical wavelength, r_e^{Opt} , follows the evolution of r_e^{UV} for the LAEs at $z \simeq 2$, suggesting, again, that the choice of the observed wavelength gives no significant impact on the galaxy size. In addition, we plot r_e^{Opt} at $z \simeq 0 - 1$ in Figure 9. Although there are a few LAEs at $z \simeq 0 - 1$ falling in the $L_{UV} = 0.12 - 1 L_{z=3}^*$ bin, we infer r_e^{Opt} by extrapolating the size-luminosity relation in Figure 8. The r_e^{Opt} is $\simeq 2$ kpc at $z \simeq 0 - 1$, supporting the size evolution of LAEs from $r_e \simeq 0.5$ kpc at $z \simeq 4 - 7$.

Figure 9 compares the effective radii for our and previous studies on LAEs, Taniguchi et al. (2009), Gronwall et al. (2011), Bond et al. (2012), Malhotra et al. (2012), Guaita et al. (2015), Hagen et al. (2016), Kobayashi et al. (2016), and Paulino-Afonso et al. (2018). Note that the median and the error bars of r_e in $L_{UV} = 0.12 - 1 L_{z=3}^*$ are re-calculated for previous studies which give the information of r_e and M_{UV} for individual sources. As found in Figure 9, most r_e measurements of previous studies are broadly consistent with the best-fit $r_e(z)$ function obtained in our LAE sample. The effective radius of Taniguchi et al. (2009), Malhotra et al. (2012), and Paulino-Afonso et al. (2018) is slightly higher than our r_e measurements. Among the studies with r_e slightly

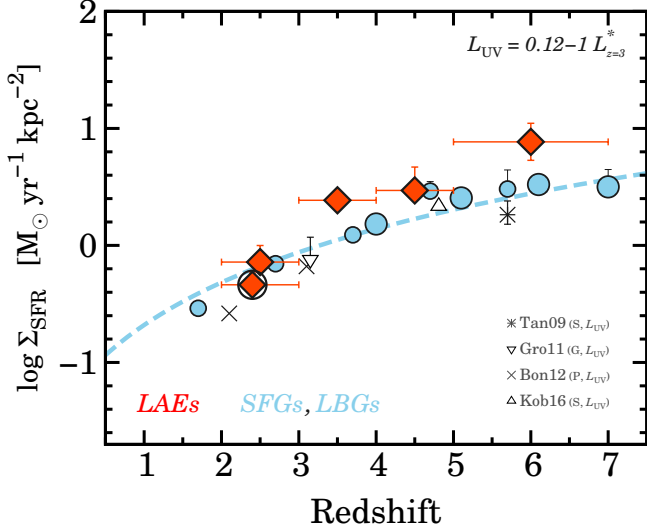


FIG. 10.— Same as Figure 9, but for the SFR SD, Σ_{SFR} . The cyan dashed curve represents the Σ_{SFG} evolution calculated with an SFR of $5 M_{\odot}/\text{yr}$ and the best-fit r_e function in Figure 9. In contrast to Paper I, the SFR for the LBGs is not corrected for dust extinction for a fair comparison with the LAEs.

higher than ours, Malhotra et al. (2012) and Paulino-Afonso et al. (2018) do not provide the r_e and M_{UV} table, which is unable us to re-calculate the median r_e in the L_{UV} range. In Section 7, we discuss the difference in the galaxy size growth rates for LAEs between previous studies and ours.

6.5. SFR Surface Density

Figure 10 presents the redshift evolution of SFR SD, Σ_{SFR} , which is one of the size-relevant quantities. The SFR SD is derived with r_e by

$$\Sigma_{\text{SFR}} [M_{\odot} \text{ yr}^{-1} \text{ kpc}^{-2}] = \frac{\text{SFR}_{\text{UV}}/2}{\pi r_e^2}. \quad (3)$$

We compute SFRs at the rest-frame UV wavelength from L_{UV} using the relation of Kennicutt (1998),

$$\text{SFR}_{\text{UV}} [M_{\odot} \text{ yr}^{-1}] = 1.4 \times 10^{-28} L_{\nu} [\text{erg s}^{-1} \text{ Hz}^{-1}]. \quad (4)$$

For all the populations, we do not take into account the dust extinction, $E(B - V)$, due to the difficulty in estimating $E(B - V)$ from e.g., spectral slopes of the rest-frame UV continuum emission, for typically faint LAEs.

As shown in Figure 10, Σ_{SFR} for the SFGs and LBGs gradually increases from $z \simeq 1$ to $z \simeq 7$. In Figure 10, we depict the Σ_{SFR} evolution curve of the SFGs and LBGs using Equation (3) with the inputs of the best-fit function of $r_e(z)$ in Section 6.5 and the SFR estimated from the L_{UV} value via Equation (4). We find that the LAEs in our and previous studies (Taniguchi et al. 2009; Gronwall et al. 2011; Bond et al. 2012; Kobayashi et al. 2016) follows the Σ_{SFR} evolutionary trend.

7. DISCUSSION

7.1. LAE size evolves or not?

One of the most striking features that are different from results in previous studies is the size growth rate

for LAEs. Our analysis has suggested that LAEs evolve in r_e similar to SFGs and LBGs (Section 6.4 and Figure 9). In contrast, some previous studies have reported that the r_e of LAEs is almost constant over the cosmic time of $z \simeq 2 - 6$ (e.g., Malhotra et al. 2012, Paulino-Afonso et al. 2018). A potential source making the difference is the binning of the galaxy luminosity (or galaxy mass) in galaxy samples. For a fair r_e comparison, an identical L_{UV} range should be applied to 1) the comparison samples (SFGs and LBGs in this case) and 2) LAEs. As shown below, the r_e comparison in the previous studies is probably affected by the L_{UV} heterogeneity.

To demonstrate the importance of the L_{UV} binning, we compare the size growth rate of our LAE sample with that of Malhotra et al. (2012) and Paulino-Afonso et al. (2018) by matching the $EW_{0,\text{Ly}\alpha}$ and L_{UV} ranges. The left panel of Figure 11 shows the result of Malhotra et al. We re-sample our LAEs with a $\text{Ly}\alpha$ EW limit of $EW_{0,\text{Ly}\alpha} > 15 \text{ \AA}$ and without a L_{UV} cut which are similar to the selection criteria of Malhotra et al. In these $EW_{0,\text{Ly}\alpha}$ and L_{UV} ranges, we find that the r_e evolution of our re-sampled LAEs broadly agrees with that of Malhotra et al. Interestingly, Malhotra et al.’s data points appear to follow the size evolution curve of the SFGs and LBGs, contrary to Malhotra et al.’s report. According to the r_e - L_{UV} relation of SFGs and LBGs (e.g., Paper I; Mosleh et al. 2012; Ono et al. 2013; van der Wel et al. 2014), the size evolution curve is shifted along the r_e direction with changing a L_{UV} range. In the case that the L_{UV} range is not matched, one could identify a false difference in the size evolution curves between the comparison samples and LAEs. Thus, the conclusion of the no r_e evolution in Malhotra et al. would be caused mostly by the L_{UV} difference between LAEs and comparison samples.

The right panel of Figure 11 shows the result of Paulino-Afonso et al. We re-sample our LAEs with a $\text{Ly}\alpha$ EW limit of $EW_{0,\text{Ly}\alpha} > 50 \text{ \AA}$ and without a L_{UV} cut which are similar to the selection criteria of Paulino-Afonso et al. As shown in the right panel of Figure 11, we reproduce a nearly constant effective radius at $r_e \simeq 0.5$ kpc that matches well the size evolution curve of Paulino-Afonso et al. However, we find a selection bias in this re-sampled LAEs and Paulino-Afonso et al.’s sample (see Figure 3 and Paulino-Afonso et al.’s Table 1). In general astronomical surveys, faint sources tend to be more detectable than bright ones at low- z . According to the r_e - L_{UV} relation, one could see galaxy sizes that are biased to small r_e at low- z and large r_e at high- z , if no L_{UV} binning is applied. Moreover, the relatively high $\text{Ly}\alpha$ EW limit of $EW_{0,\text{Ly}\alpha} > 50 \text{ \AA}$ tends to exclude L_{UV} -brighter LAEs at lower- z due to the $EW_{0,\text{Ly}\alpha}$ - L_{UV} anticorrelation (Ando et al. 2006), more severely enhancing the selection bias. Such a different L_{UV} range would compensate the intrinsic size evolution of LAEs.

For these reasons, the size evolution should be compared at a given luminosity. In our study, L_{UV} is confined to $L_{\text{UV}} = 0.12 - 1 L_{z=3}^*$ for a fair r_e comparison between our samples of LAEs, SFGs, and LBGs. In this L_{UV} range, we find that LAEs show the size evolution even in the literature LAE samples (i.e., data points of Gronwall et al. 2011, Bond et al. 2012 and Hagen et al. 2016 in Figure 9). In addition to the L_{UV} binning, note that

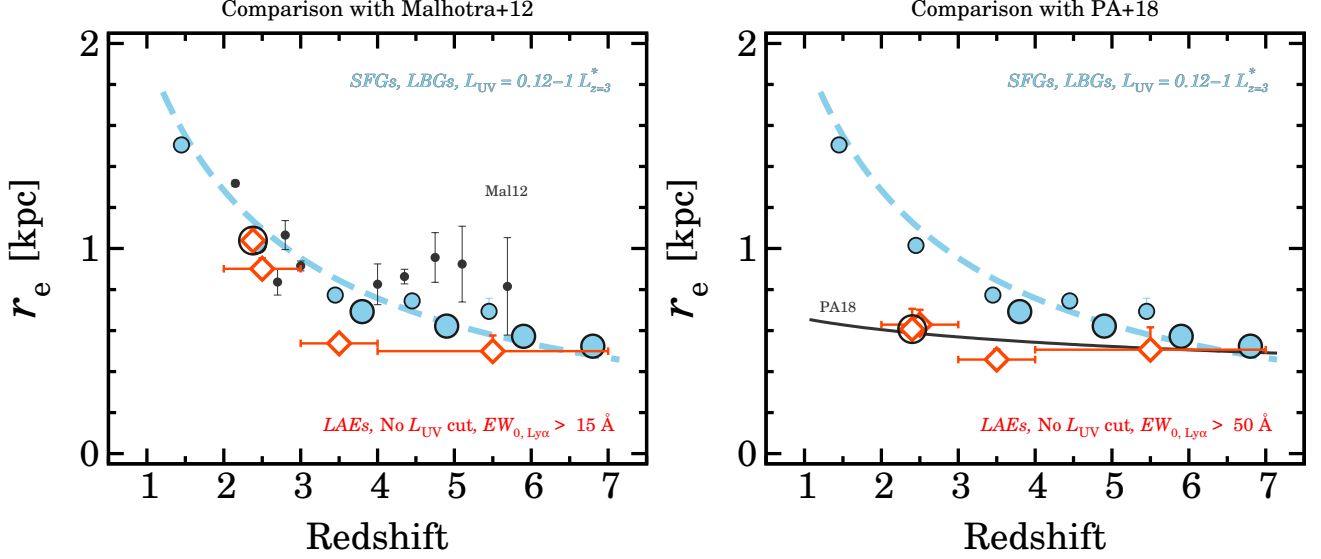


FIG. 11.— Same as Figure 9, but for a comparison with the size evolution with [Malhotra et al. \(2012\)](#) (left panel) and [Paulino-Afonso et al. \(2018\)](#) (right panel). The black filled circles indicate the r_e measurements in [Malhotra et al. \(2012\)](#). The black solid line denotes the no size evolution curve of $r_e \propto (1+z)^{-0.21}$ in [Paulino-Afonso et al. \(2018\)](#) which is matched to our r_e data point for LAEs at $z = 4 - 7$. The open diamonds represent our LAEs that are re-sampled with $EW_{0,Ly\alpha} > 15 \text{ \AA}$ (left panel) and $EW_{0,Ly\alpha} > 50 \text{ \AA}$ (right panel). In both cases, no L_{UV} cut is adopted.

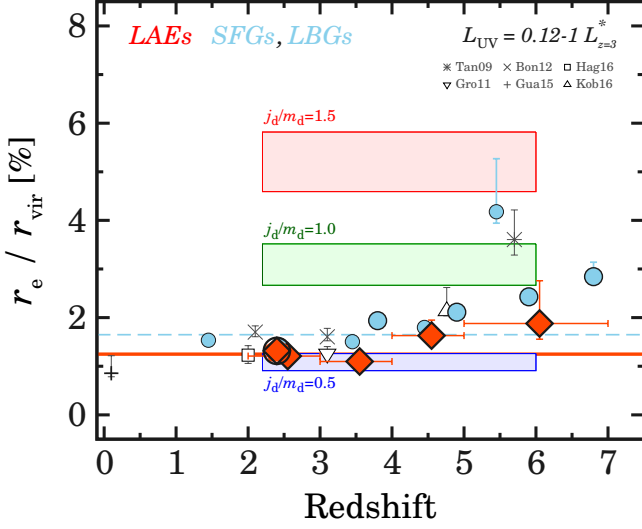


FIG. 12.— Same as Figure 9, but for the SHSR, r_e/r_{vir} . The magenta solid and cyan dashed horizontal lines indicate weighted means of $\langle r_e/r_{vir} \rangle$ for the LAEs and for the SFGs and LBGs, respectively. The virial mass of host DM halos is derived from the results of [Behroozi et al. \(2013\)](#). The red, green, and blue shaded areas illustrate the regions of $j_d/m_d = 1.5$, 1.0, and 0.5, respectively (see Section 7.2 for details).

we match the choice of statistics (i.e. the median), the technique to measure r_e (i.e. GALFIT), and the band of the *HST* images to trace the stellar continuum emission (see Section 4). Our systematic analysis has identified the size evolution for LAEs similar to SFGs and LBGs.

7.2. Implications for the galaxy disk formation of LAEs

As indicated by the low Sérsic index of $n \simeq 1 - 1.5$ in Section 6.1, we have revealed that LAEs typically have a disk-like SB profile in the stellar continuum emission. In

addition, the r_e distribution and its width are consistent with a picture that stellar components of LAEs is formed in host DM halos through galaxy disk formation models (Section 6.2). To provide the implications of the galaxy disk formation of LAEs, we infer the stellar-to-halo size ratios (SHSRs) that are defined as the ratio of r_e/r_{vir} , where r_{vir} the virial radius of a host DM halo.

Figure 12 plots r_e/r_{vir} as a function of redshift in the luminosity range of $L_{UV} = 0.12 - 1 L_{z=3}^*$. The technique to estimate the SHSRs is the same as that in [Kawamata et al. \(2015\)](#) and [Paper I](#). The r_{vir} value is calculated by

$$r_{vir} = \left(\frac{2GM_{vir}}{\Delta_{vir}\Omega_m(z)H(z)^2} \right)^{1/3}, \quad (5)$$

where $\Delta_{vir} = 18\pi^2 + 82x - 39x^2$ and $x = \Omega_m(z) - 1$ ([Bryan & Norman 1998](#)). We obtain the virial mass of a DM halo, M_{vir} , from stellar mass, M_* , of individual galaxies by using the relation determined by the abundance matching analyses ([Behroozi et al. 2010, 2013](#)). In the M_* range for our LAEs (i.e., $\log M_*/M_\odot \simeq 9 - 10$), the assumed M_*/M_{vir} ratio varies by $\simeq \pm 0.3 - 0.4$ dex, depending on results of theoretical and observational studies (e.g., [Behroozi et al. 2018](#)). Given the weak dependence of M_{vir} on r_{vir} (Equation 5), the assumed M_*/M_{vir} ratio does not significantly affect r_e/r_{vir} and our conclusion. To estimate the stellar mass M_* , we use M_{UV} and the empirical M_*-M_{UV} relation in [Paper I](#).

In Figure 12, we find that the r_e/r_{vir} estimates for LAEs fall within the range of $r_e/r_{vir} = 1 - 2\%$ similar to the SFGs and LBGs. Interestingly, r_e/r_{vir} of the LAEs is nearly constant with redshift, albeit with the large uncertainties at $z \gtrsim 5$. The weighted means of the r_e/r_{vir} measurements at λ_{UV} are $1.25 \pm 0.09\%$ for the LAEs and $1.65 \pm 0.10\%$ for the SFGs and LBGs. For comparison, we apply this calculation to the literature LAE samples with L_{UV} (i.e., [Taniguchi et al. 2009](#); [Gronwall et al.](#)

2011; Bond et al. 2012; Guaita et al. 2015; Hagen et al. 2016; Kobayashi et al. 2016). As shown in Figure 12, our LAEs agree in r_e/r_{vir} with these literature LAE samples.

According to the galaxy disk formation models of e.g., Fall & Efstathiou (1980) and Mo et al. (1998), the SHSR is linked to the specific angular momentum, j_d/m_d . Figure 12 also shows r_e/r_{vir} regions corresponding to $j_d/m_d = 0.5, 1.0$, and 1.5 inferred from

$$\frac{r_e}{r_{\text{vir}}} = \frac{1.678}{\sqrt{2}} \left(\frac{j_d}{m_d} \lambda \right) \frac{f_R(\lambda, c_{\text{vir}}, m_d, j_d)}{\sqrt{f_c(c_{\text{vir}})}}, \quad (6)$$

where the j_d (m_d) value is a angular momentum (mass) ratio of a central disk to a host DM halo. The $f_c(c_{\text{vir}})$ and $f_R(\lambda, c_{\text{vir}}, m_d, j_d)$ are functions related to halo and baryon concentrations, respectively. The c_{vir} is the halo concentration factor. If we use λ and c_{vir} values well constrained by numerical simulations (e.g., Vitvitska et al. 2002; Davis & Natarajan 2009; Prada et al. 2012), we can constrain j_d/m_d . Figure 12 presents that our estimates of r_e/r_{vir} range from $j_d/m_d \simeq 0.5$ to $\simeq 1$. This result of $j_d/m_d \sim 0.5 - 1$ indicates that a central galaxy of LAEs acquire more than half of specific angular momentum from a host DM halo.

As presented in the previous sections, our systematic structural analyses have revealed that LAEs have the Sérsic index, the r_e distribution, the size growth rate, the SFR SD, and the SHSR that are comparable with those of SFGs and LBGs. These morphological similarities between LAEs and other galaxy populations have already been reported at $z \simeq 2 - 3$ (e.g., Hagen et al. 2016; Shimakawa et al. 2017). We confirm this similarity in the wide redshift range of $z \simeq 0 - 7$ in our large LAE sample. The results naturally indicate that the mechanism of the Ly α photon escape is related to e.g., properties of the interstellar/circum-galactic medium, e.g., the amount (e.g., Pardy et al. 2014; Shibuya et al. 2014b; Hashimoto et al. 2015), geometry (e.g., Zheng & Wallace 2013), kinematics (e.g., Herenz et al. 2016), and ionization states (e.g., Nakajima & Ouchi 2013), rather than the global galaxy morphology in the stellar components. In addition to phenomena related to non-stellar physics, the star formation history would be an important factor controlling the Ly α emissivity (e.g., Schaerer 2003). Spatially-resolved and multi-wavelength analyses need to be performed to understand the relation between stellar populations, galaxy morphological properties, and the Ly α emissivity.

7.3. Origins of Ly α halos

In this last section, we discuss the physical origins of Ly α halos with the *HST* data of the stellar components. Using our large LAE sample, we have created radial SB profiles in the rest-frame UV stellar continuum emission in the stacked *HST* images (Section 6.1). Here we compare our radial SB profile in UV with one in Ly α obtained in a MUSE IFU observation (Leclercq et al. 2017). Figure 13 presents the radial profiles in UV and the Ly α halo for LAEs at $z = 3 - 4$ in $L_{\text{UV}} = 0.12 - 1L_{z=3}^*$. The Ly α halo is a median stacked 1D profile of LAEs with the best-fit stellar continuum and halo slopes, $r_{s,\text{cont}}$ and $r_{s,\text{halo}}$ (see Leclercq et al. 2017) which fall within the ranges of $z = 3 - 4$ and $L_{\text{UV}} = 0.12 - 1L_{z=3}^*$. Consid-

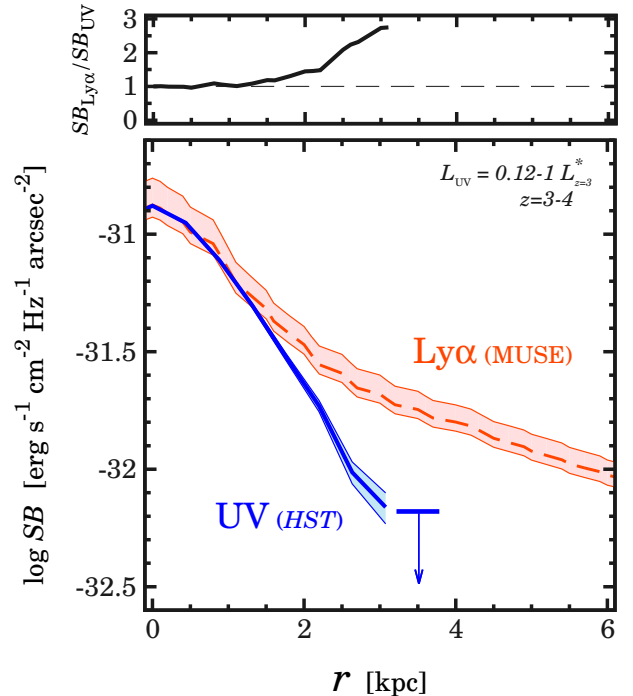


FIG. 13.— Radial SB profiles for LAEs at $z = 3 - 4$ in the L_{UV} bin of $L_{\text{UV}} = 0.12 - 1L_{z=3}^*$. The blue solid curve and red dashed curves show the median radial SB profiles derived from the rest-frame UV continuum (this study) and Ly α (Leclercq et al. 2017) emission, respectively. The shaded regions depict the standard error of each radial SB profile. The radial SB profile in the rest-frame UV continuum emission is displayed above a $\sim 5\sigma$ detection in our *HST* stacked image. The radial SB profiles in Ly α and UV are compared in the same PSF size. The top-panel presents the ratio of $SB_{\text{Ly}\alpha}$ and SB_{UV} as a function of radius.

ered the ambiguity of the Ly α escape fraction, $SB_{\text{Ly}\alpha}$ is scaled to match SB_{UV} at $r = 0$ kpc.

As shown in Figure 13, we find that SB_{UV} is lower than $SB_{\text{Ly}\alpha}$ by a factor of at least $\simeq 2 - 3$ at $r \simeq 3$ kpc. This is consistent with the reports in the literature (Steidel et al. 2011; Matsuda et al. 2012; Momose et al. 2014). This result indicates that the Ly α halo is not originated only from the recombination of the small satellite galaxies and diffuse stellar disks. The high spatial resolution of the *HST* images enables us to investigate the central regions of the Ly α halo, less affected by e.g., the sky oversubtraction and flat-fielding effects (Feldmeier et al. 2013; Momose et al. 2016). Interestingly, the SB deficit in UV compared to Ly α is shown in the vicinity of the galaxy center, at $r \simeq 1 - 2$ kpc. The high spatial resolution radial profiles would provide important constraints on the radiation budget of the several Ly α halo formation mechanisms (e.g., Dijkstra & Kramer 2012; Lake et al. 2015; Mas-Ribas & Dijkstra 2016; Mas-Ribas et al. 2017a,b).

8. SUMMARY AND CONCLUSIONS

We investigate the redshift evolution of radial SB profiles and effective radii, r_e , of the rest-frame UV and optical stellar continua for 9119 LAEs at $z \simeq 0 - 8$ that are compiled from literature wide-field NB, MB, and MUSE/IFU data. This LAE sample is the largest for studies of LAE galaxy structures in the wide-redshift

range of $z \simeq 0 - 8$. Using the deep extra-galactic legacy data of *HST*, we measure the structural quantities for the LAEs to make a comparison with $\simeq 180,000$ sources of photo- z SFGs and LBGs at $z \simeq 0 - 10$ in Paper I. The structural quantities of the LAEs, SFGs, and LBGs are obtained in the same techniques of the size measurement, the same choice of statistics, the same bands of the *HST* images, and the same UV-continuum luminosity range, allowing to evaluate the redshift evolution of galaxy structures with no significant systematics.

The main results of this study are summarized as follows.

1. The analyses of the radial SB profiles in individual and stacked *HST* images reveal that the Sérsic index is almost constant at $n \simeq 1 - 1.5$ for LAEs over the cosmic time. The Sérsic index measurements suggest that LAEs typically have a disk-like SB profile in the stellar continuum emission independent of redshift.
2. The r_e distribution shape of LAEs is represented by log-normal functions. The standard deviation of the log-normal r_e distribution, $\sigma_{\ln r_e}$, is $\sigma_{\ln r_e} \simeq 0.45 - 0.75$ for LAEs which is comparable to that of the DM spin parameter, $\sigma_{\ln \lambda} \sim 0.5 - 0.6$. The similarity of the distribution shapes and standard deviations of r_e and λ would imply that galaxy sizes of stellar components are associated with the host DM halo kinematics.
3. The size-luminosity relation of the LAEs monotonically decreases towards high- z , following the size-luminosity relations of SFGs and LBGs. The median r_e values of the LAEs significantly evolve as $r_e \propto (1+z)^{-1.37 \pm 0.65}$, similar to those of the SFGs and LBGs in the same luminosity range of $L_{UV} = 0.12 - 1L_{z=3}^*$. This size growth rate is in contrast with the claims of no evolution made by previous studies whose LAE samples are probably biased to faint sources at low redshift.
4. Combining our stellar r_e measurements with host DM halo radii, r_{vir} , estimated from an abundance matching study, we obtain a median value of

$r_e/r_{vir} = 1 - 3\%$, which is nearly constant at $z \simeq 2 - 7$, similar to SFGs and LBGs. If we assume the disk formation model of Mo et al. (1998), our r_e/r_{vir} estimates indicate that a central LAE acquires more than a half of specific angular momentum from their host DM halo, $j_d/m_d \simeq 0.5 - 1$.

5. We compare stacked radial SB profiles in the rest-frame UV and Ly α (Leclercq et al. 2017), SB_{UV} and $SB_{Ly\alpha}$. The comparison reveals that SB_{UV} is lower than $SB_{Ly\alpha}$ by a factor of $\gtrsim 2-3$ at $r \simeq 3$ kpc from the galaxy center. This deficit in SB_{UV} suggests that the flux contribution of satellite small galaxies is $\lesssim 30 - 50\%$ to the Ly α halos, which is consistent with estimates of ground-based telescopes. Interestingly, this deficit is found in the vicinity of the galaxy center, at $r \simeq 1 - 2$ kpc. The high spatial resolution radial profiles of the stellar continuum would provide important constraints on the Ly α halo formation mechanisms.

Our structural analyses have revealed that the Sérsic index, the r_e distribution, the size growth rate, the SFR SD, and the SHSR of the LAEs are comparable with those of the SFGs and LBGs. These morphological similarities between stellar components of the LAEs, SFGs, and LBGs would indicate that the Ly α photon escape is controlled by the non-stellar physics such as geometry, kinematics, and ionization states of the interstellar/circum-galactic medium.

We thank the anonymous referee for constructive comments and suggestions. This work is based on observations taken by the 3D-HST Treasury Program (GO 12177 and 12328) and CANDELS Multi-Cycle Treasury Program with the NASA/ESA HST, which is operated by the Association of Universities for Research in Astronomy, Inc., under NASA contract NAS5-26555. Support for this work was provided by NASA through an award issued by JPL/Caltech. This work is supported by KAKENHI 16J07046 and 15H02064 through Japan Society for the Promotion of Science, and World Premier International Research Center Initiative, MEXT, Japan.

Facilities: HST (ACS, WFC3).

REFERENCES

- Ando, M., Ohta, K., Iwata, I., Akiyama, M., Aoki, K., & Tamura, N. 2006, *ApJ*, 645, L9
- Bacon, R., et al. 2010, in *Proc. SPIE*, Vol. 7735, Ground-based and Airborne Instrumentation for Astronomy III, 773508
- Bacon, R., et al. 2015, *A&A*, 575, A75
- , 2017, *A&A*, 608, A1
- Barden, M., Häußler, B., Peng, C. Y., McIntosh, D. H., & Guo, Y. 2012, *MNRAS*, 422, 449
- Barger, A. J., Cowie, L. L., & Wold, I. G. B. 2012, *ApJ*, 749, 106
- Barnes, J., & Efstathiou, G. 1987, *ApJ*, 319, 575
- Beckwith, S. V. W., et al. 2006, *AJ*, 132, 1729
- Behroozi, P., Wechsler, R., Hearin, A., & Conroy, C. 2018, *ArXiv e-prints*, arXiv:1806.07893
- Behroozi, P. S., Conroy, C., & Wechsler, R. H. 2010, *ApJ*, 717, 379
- Behroozi, P. S., Wechsler, R. H., & Conroy, C. 2013, *ApJ*, 770, 57
- Bertin, E., & Arnouts, S. 1996, *A&AS*, 117, 393
- Bezanson, R., van Dokkum, P. G., Tal, T., Marchesini, D., Kriek, M., Franx, M., & Coppi, P. 2009, *ApJ*, 697, 1290
- Blanc, G. A., et al. 2011, *ApJ*, 736, 31
- Bond, N. A., Gawiser, E., Gronwall, C., Ciardullo, R., Altmann, M., & Schawinski, K. 2009, *ApJ*, 705, 639
- Bond, N. A., Gawiser, E., Guaita, L., Padilla, N., Gronwall, C., Ciardullo, R., & Lai, K. 2012, *ApJ*, 753, 95
- Bouwens, R. J., Illingworth, G. D., Blakeslee, J. P., Broadhurst, T. J., & Franx, M. 2004, *ApJ*, 611, L1
- Bouwens, R. J., Illingworth, G. D., Oesch, P. A., Atek, H., Lam, D., & Stefanon, M. 2017, *ApJ*, 843, 41
- Bouwens, R. J., et al. 2011, *ApJ*, 737, 90
- Brooks, A. M., Governato, F., Quinn, T., Brook, C. B., & Wadsley, J. 2009, *ApJ*, 694, 396
- Bryan, G. L., & Norman, M. L. 1998, *ApJ*, 495, 80
- Bullock, J. S., Dekel, A., Kolatt, T. S., Kravtsov, A. V., Klypin, A. A., Porciani, C., & Primack, J. R. 2001, *ApJ*, 555, 240
- Caruana, J., et al. 2018, *MNRAS*, 473, 30
- Ciardullo, R., et al. 2012, *ApJ*, 744, 110
- Cowie, L. L., Barger, A. J., & Hu, E. M. 2010, *ApJ*, 711, 928
- Cowie, L. L., Hu, E. M., & Songaila, A. 2011, *ApJ*, 735, L38
- Davis, A. J., & Natarajan, P. 2009, *MNRAS*, 393, 1498
- Dayal, P., & Ferrara, A. 2018, *ArXiv e-prints*, arXiv:1809.09136
- Deharveng, J.-M., et al. 2008, *ApJ*, 680, 1072
- Dijkstra, M. 2017, *ArXiv e-prints*, arXiv:1704.03416
- Dijkstra, M., & Kramer, R. 2012, *MNRAS*, 424, 1672
- Ellis, R. S., et al. 2013, *ApJ*, 763, L7
- Fall, S. M., & Efstathiou, G. 1980, *MNRAS*, 193, 189

- Fall, S. M., & Romanowsky, A. J. 2018, ArXiv e-prints
 Feldmeier, J. J., et al. 2013, ApJ, 776, 75
 Ferguson, H. C., et al. 2004, ApJ, 600, L107
 Finkelstein, S. L., Rhoads, J. E., Malhotra, S., & Grogin, N. 2009, ApJ, 691, 465
 Grazian, A., et al. 2012, A&A, 547, A51
 Grogin, N. A., et al. 2011, ApJS, 197, 35
 Gronwall, C., Bond, N. A., Ciardullo, R., Gawiser, E., Altmann, M., Blanc, G. A., & Feldmeier, J. J. 2011, ApJ, 743, 9
 Gronwall, C., et al. 2007, ApJ, 667, 79
 Guaita, L., et al. 2015, A&A, 576, A51
 Hagen, A., et al. 2014, ApJ, 786, 59
 —. 2016, ApJ, 817, 79
 Harikane, Y., et al. 2016, ApJ, 821, 123
 Hashimoto, T., et al. 2015, ApJ, 812, 157
 Hayashino, T., et al. 2004, AJ, 128, 2073
 Hayes, M., et al. 2014, ApJ, 782, 6
 Hearin, A., Behroozi, P., Kravtsov, A., & Moster, B. 2017, ArXiv e-prints
 Herenz, E. C., et al. 2016, A&A, 587, A78
 —. 2017, A&A, 606, A12
 Holwerda, B. W., Bouwens, R., Oesch, P., Smit, R., Illingworth, G., & Labbe, I. 2015, ApJ, 808, 6
 Hu, E. M., Cowie, L. L., Barger, A. J., Capak, P., Kakazu, Y., & Trouille, L. 2010, ApJ, 725, 394
 Hu, W., et al. 2017, ApJ, 845, L16
 Huang, K.-H., Ferguson, H. C., Ravindranath, S., & Su, J. 2013, ApJ, 765, 68
 Huang, K.-H., et al. 2017, ApJ, 838, 6
 Illingworth, G. D., et al. 2013, ApJS, 209, 6
 Itoh, R., et al. 2018, ArXiv e-prints, arXiv:1805.05944
 Jiang, L., et al. 2013, ApJ, 773, 153
 —. 2016, ApJ, 816, 16
 Kawamata, R., Ishigaki, M., Shimasaku, K., Oguri, M., & Ouchi, M. 2015, ApJ, 804, 103
 Kawamata, R., Ishigaki, M., Shimasaku, K., Oguri, M., Ouchi, M., & Tanigawa, S. 2018, ApJ, 855, 4
 Kelvin, L. S., et al. 2012, MNRAS, 421, 1007
 Kennicutt, Jr., R. C. 1998, ARA&A, 36, 189
 Kobayashi, M. A. R., et al. 2016, ApJ, 819, 25
 Koekemoer, A. M., et al. 2011, ApJS, 197, 36
 Konno, A., Ouchi, M., Nakajima, K., Duval, F., Kusakabe, H., Ono, Y., & Shimasaku, K. 2016, ApJ, 823, 20
 Lake, E., Zheng, Z., Cen, R., Sadoun, R., Momose, R., & Ouchi, M. 2015, ApJ, 806, 46
 Leclercq, F., et al. 2017, A&A, 608, A8
 Malhotra, S., Rhoads, J. E., Finkelstein, S. L., Hathi, N., Nilsson, K., McLinden, E., & Pirzkal, N. 2012, ApJ, 750, L36
 Mas-Ribas, L., & Dijkstra, M. 2016, ApJ, 822, 84
 Mas-Ribas, L., Dijkstra, M., Hennawi, J. F., Trenti, M., Momose, R., & Ouchi, M. 2017a, ApJ, 841, 19
 Mas-Ribas, L., Hennawi, J. F., Dijkstra, M., Davies, F. B., Stern, J., & Rix, H.-W. 2017b, ApJ, 846, 11
 Matsuda, Y., et al. 2012, MNRAS, 425, 878
 Matthee, J., Sobral, D., Oteo, I., Best, P., Smail, I., Röttgering, H., & Paulino-Afonso, A. 2016, MNRAS, 458, 449
 Matthee, J., Sobral, D., Santos, S., Röttgering, H., Darvish, B., & Mobasher, B. 2015, MNRAS, 451, 400
 McLure, R. J., et al. 2013, MNRAS, 428, 1088
 Mo, H. J., Mao, S., & White, S. D. M. 1998, MNRAS, 295, 319
 Momose, R., et al. 2014, MNRAS, 442, 110
 —. 2016, MNRAS, 457, 2318
 Mosleh, M., Williams, R. J., & Franx, M. 2013, ApJ, 777, 117
 Mosleh, M., et al. 2012, ApJ, 756, L12
 Murayama, T., et al. 2007, ApJS, 172, 523
 Nakajima, K., & Ouchi, M. 2013, ArXiv e-prints
 Nakajima, K., et al. 2012, ApJ, 745, 12
 Oesch, P. A., et al. 2015, ApJ, 804, L30
 Okamura, T., Shimasaku, K., & Kawamata, R. 2018, ApJ, 854, 22
 Oke, J. B., & Gunn, J. E. 1983, ApJ, 266, 713
 Ono, Y., et al. 2012, ApJ, 744, 83
 —. 2013, ApJ, 777, 155
 Östlin, G., et al. 2014, ApJ, 797, 11
 Ota, K., et al. 2017, ApJ, 844, 85
 Ouchi, M., et al. 2008, ApJS, 176, 301
 —. 2009, ApJ, 706, 1136
 —. 2010, ApJ, 723, 869
 Overzier, R. A., et al. 2008, ApJ, 673, 143
 Pardy, S. A., et al. 2014, ApJ, 794, 101
 Paulino-Afonso, A., Sobral, D., Buitrago, F., & Afonso, J. 2017, MNRAS, 465, 2717
 Paulino-Afonso, A., et al. 2018, MNRAS, 476, 5479
 Peng, C. Y., Ho, L. C., Impey, C. D., & Rix, H.-W. 2002, AJ, 124, 266
 —. 2010, AJ, 139, 2097
 Pentericci, L., et al. 2018, ArXiv e-prints, arXiv:1808.01847
 Pirzkal, N., Malhotra, S., Rhoads, J. E., & Xu, C. 2007, ApJ, 667, 49
 Planck Collaboration et al. 2016, A&A, 594, A13
 Prada, F., Klypin, A. A., Cuesta, A. J., Betancort-Rijo, J. E., & Primack, J. 2012, MNRAS, 423, 3018
 Rauch, M., et al. 2008, ApJ, 681, 856
 Schaerer, D. 2003, A&A, 397, 527
 Sérsic, J. L. 1963, Boletín de la Asociación Argentina de Astronomía La Plata Argentina, 6, 41
 —. 1968, Atlas de Galaxias Australes
 Shen, S., Mo, H. J., White, S. D. M., Blanton, M. R., Kauffmann, G., Voges, W., Brinkmann, J., & Csabai, I. 2003, MNRAS, 343, 978
 Shibuya, T., Kashikawa, N., Ota, K., Iye, M., Ouchi, M., Furusawa, H., Shimasaku, K., & Hattori, T. 2012, ApJ, 752, 114
 Shibuya, T., Ouchi, M., & Harikane, Y. 2015, ApJS, 219, 15
 Shibuya, T., Ouchi, M., Kubo, M., & Harikane, Y. 2016, ApJ, 821, 72
 Shibuya, T., Ouchi, M., Nakajima, K., Yuma, S., Hashimoto, T., Shimasaku, K., Mori, M., & Umemura, M. 2014a, ApJ, 785, 64
 Shibuya, T., et al. 2014b, ApJ, 788, 74
 Shimakawa, R., et al. 2017, MNRAS, 468, 1123
 Shioya, Y., et al. 2009, ApJ, 700, 899
 Skelton, R. E., et al. 2014, ApJS, 214, 24
 Smit, R., et al. 2015, ApJ, 801, 122
 Sobral, D., Santos, S., Matthee, J., Paulino-Afonso, A., Ribeiro, B., Calhau, J., & Khostovan, A. A. 2017a, ArXiv e-prints
 Sobral, D., et al. 2017b, MNRAS, 466, 1242
 Somerville, R. S., et al. 2018, MNRAS, 473, 2714
 Steidel, C. C., Adelberger, K. L., Giavalisco, M., Dickinson, M., & Pettini, M. 1999, ApJ, 519, 1
 Steidel, C. C., Bogosavljević, M., Shapley, A. E., Kollmeier, J. A., Reddy, N. A., Erb, D. K., & Pettini, M. 2011, ApJ, 736, 160
 Taniguchi, Y., et al. 2009, ApJ, 701, 915
 van der Wel, A., et al. 2014, ApJ, 788, 28
 Venemans, B. P., et al. 2005, A&A, 431, 793
 Vitvitska, M., Klypin, A. A., Kravtsov, A. V., Wechsler, R. H., Primack, J. R., & Bullock, J. S. 2002, ApJ, 581, 799
 Warren, M. S., Quinn, P. J., Salmon, J. K., & Zurek, W. H. 1992, ApJ, 399, 405
 Wisotzki, L., et al. 2016, A&A, 587, A98
 Wold, I. G. B., Barger, A. J., & Cowie, L. L. 2014, ApJ, 783, 119
 Wold, I. G. B., Finkelstein, S. L., Barger, A. J., Cowie, L. L., & Rosenwasser, B. 2017, ApJ, 848, 108
 Xu, C., et al. 2007, AJ, 134, 169
 Xue, R., et al. 2017, ApJ, 837, 172
 Yang, H., Malhotra, S., Rhoads, J. E., Leitherer, C., Wofford, A., Jiang, T., & Wang, J. 2017a, ApJ, 838, 4
 Yang, H., et al. 2017b, ApJ, 844, 171
 Zheng, Z., & Wallace, J. 2013, ArXiv e-prints
 Zheng, Z.-Y., et al. 2017, ApJ, 842, L22